Journal of Power Sources 660 (2025) 238538

Contents lists available at ScienceDirect

Journal of Power Sources

journal homepage: www.elsevier.com/locate/jpowsour

Cerium in-plane transport in PEM fuel cells during real-world automotive operations: experimental and dynamic modelling analysis

Francesco Verducci [a,*], Livio Cultrera [a], Elena Colombo [a,**], Aixeen Manuel Fontanilla [b], Francesco Casamichiela [b], Davide Mazzucconi [b], Andrea Pola [b], Andrea Casalegno [a], Andrea Baricci [a]

[a] Politecnico di Milano, Department of Energy, Via Lambruschini 4, Milano, 20156, Italy
[b] Politecnico di Milano, Department of Energy, Via La Masa 34, Milano, 20156, Italy

HIGHLIGHTS

- 1D Ce transport model calibration and validation on tailored and literature data.
- Gradients of Ce concentration, ionic potential and water activity are considered.
- Coupling between the 1D in-plane Ce transport and a 1+1D PEMFC performance models.
- Cerium redistribution after hundreds hours of dynamic drive cycles is predicted.
- Modelling shows the key role played by ionic potential and water content.

ARTICLE INFO

Keywords:
Radical scavenger
Cerium migration
Ion transport
Dynamic modelling
Polymer electrolyte membrane fuel cell
X-ray fluorescence

ABSTRACT

Cerium is an additive adopted in polymer electrolyte membrane fuel cells to extend membrane lifetime, but its mobility remains a challenge. A cerium transport model accounting for diffusion, migration and water activity gradient is developed. Diffusion coefficient is calibrated on literature data, as the effect of Ce ion-exchange fraction on protonic conductivity and membrane water uptake; Einstein relation is used for the migration coefficient. Validation is conducted on migration profiles obtained via hydrogen pump tests, quantified through X-ray fluorescence. Trends under different temperatures, relative humidities and initial cerium contents are reproduced. Tailored tests investigate how the water activity gradient affects Ce transport. Furthermore, a 1+1D fuel cell performance model is exploited to determine the initial and time-integral mean values of the operating variables that characterize the current steps of a dynamic load cycle, then provided to the Ce transport model. The experimentally measured planar radical scavenger redistributions, after hundreds of hours of single-cell automotive-representative operations, are predicted from air-inlet to outlet. Cerium accumulates towards air-inlet and depletes at middle/outlet; the modelling analysis identifies the building-up in the region of lowest ionic potential and water content. Succeeding in predictions, this model can support the development of strategies to improve durability.

1. Introduction

Polymer electrolyte membrane fuel cells (PEMFCs) represent a promising alternative to conventional internal combustion engines for the decarbonization of heavy-duty transport sector (i.e. trucks, buses, ships) thanks to the high efficiency, noise-free operation, fast start-up and fast refuelling [1]. Nevertheless, the low durability of the components of the membrane electrode assembly (MEA) limits the penetration of the technology into the market. In particular, the membrane, composed of perfluorosulfonic acid (PFSA) polymer, is subjected to both chemical and mechanical degradation [2–4]. The former is driven by OH/OOH radicals [5–7], which are mostly formed in the membrane due

* Corresponding author.
** Corresponding author.
E-mail addresses: francesco.verducci@polimi.it (F. Verducci), elena.colombo@polimi.it (E. Colombo).

https://doi.org/10.1016/j.jpowsour.2025.238538
Received 4 August 2025; Received in revised form 17 September 2025; Accepted 28 September 2025
Available online 15 October 2025

to the decomposition of hydrogen peroxide (H_2O_2) and that attack the ionomer chains compromising their stability and leading to membrane thinning [8,9]. Mechanical degradation, on the other hand, is induced by hydration/dehydration cycles and relative humidity (RH) cycling, which lead to the formation of pinholes, microcracks and delamination [10,11]. An effective strategy commonly adopted to mitigate the chemical degradation of the membrane consists in the introduction of radical scavengers that can directly neutralize the OH/OOH radicals [2,12]. In this scenario, cerium (Ce) cations or oxides (e.g. ceria nanoparticles) are commonly adopted in PEMFC thanks to their ability to rapidly neutralize the radicals thus increasing MEA lifetime [2,8]. Unfortunately, during operation, as stated in the literature, cerium ions migrate in the through-plane direction [13] due to gradients in concentration [12], ionic potential [14,15] and relative humidity [16]. Cerium migration into the cathode catalyst layer (CCL) negatively affects PEMFC performance by diminishing ionomer conductivity [14]. Moreover, as suggested by recent works in the literature [9,17,18], cation contamination can reduce oxygen diffusion through the ionomer, thus introducing additional performance losses at high current density.

Cerium ions transport over the in-plane direction of the MEA active area has received less attention but the previous work of Colombo et al. [9] proposed that the planar potential gradients established under automotive-like operating conditions, coupled with water content (λ) gradients, can lead to cerium redistribution. Such redistribution was experimentally observed after 1000 h of operation under the conditions of the Dynamic Load Cycle (DLC) protocol – defined in the framework of the European ID-FAST project [19]. An elemental analysis, carried out by means of micro X-ray fluorescence (XRF) technique [20], revealed a significant cerium accumulation at the air inlet region, characterized by the driest operating conditions, and a depletion at the air outlet region, characterized instead by the highest water content. This result, coherent with the work of Lai et al. [21], allowed to explain the heterogeneous performance decay experimentally observed and, in particular, the more relevant increase of the pressure-independent component of the oxygen mass transport resistance in the region with cerium accumulation [19]. After 1000 h of the complete ID-FAST DLC protocol, the mass transport resistance at air inlet, where Ce build-up was observed, increased three times more with respect to the average fuel cell behaviour [9]. This effect, as suggested in the literature [14,17,18], may be associated with the more tortuous oxygen pathway induced by cation contamination. Moreover, cerium depletion at air outlet can explain the more evident increase in the hydrogen crossover current showed by this portion of the MEA [9], which can be linked to a more pronounced chemical degradation of the PFSA membrane promoted by a lower radical scavenger content. After 1000 h of operation, the hydrogen crossover current at the air outlet region, was found to be 20 % higher than the other regions of the cell [9]. In summary, the planar radical scavenger redistribution has a double impact on both PEMFC performance and durability: (i) where Ce accumulates, additional performance losses can cause membrane and catalyst layer contamination [9,17,18]; (ii) the degradation rate of the ionomer where Ce is depleted is instead locally accelerated, hence the membrane service life is reduced [21].

Therefore, stabilizing cerium within the membrane over the entire fuel cell lifetime is critical to achieve the 30′000 h durability target set by the United States Department of Energy (DoE) for the heavy-duty transportation sector [1]. To do that, both material-based solutions [22,23] and proper system control-based strategies can be developed. However, this requires a deeper understanding of the drivers responsible for cerium migration and of the operating conditions which influence its transport. In this scenario, reliable numerical models can play a key role. To the authors' best knowledge, there are just few examples of cerium transport model: based on the Nernst-Planck equation, Baker et al. [14] developed a migration model to fit on XRF profiles the mobility coefficients (i.e. both diffusion and migration) as a function of water content, showing the strong effect of RH and ionic potential gradient on cerium transport. Ehlinger et al. [8] coupled instead a cerium transport model with a full-cell transient, performance and durability model to predict the impact of cerium transport in the through-plane direction. Nevertheless, no one has implemented an in-plane cerium transport model to predict an experimentally observed planar Ce migration due to real-world PEMFC operation.

To fill this gap, the aim of this work is to develop and validate a 1D in-plane cerium transport model over experimental data available in the literature [14] and tailored data gathered via membrane hydrogen pump and humidity gradient tests, the former according to the methodology already proposed by Baker et al. [14]. After that, the 1D in-plane cerium transport model is coupled with a 1+1D transient non-isothermal and multiphase PEMFC performance model, already described and validated in Verducci et al. [24], to develop an innovative framework able to simulate a realistic in-plane cerium redistribution. Hundreds of hours of operation under the operating conditions of a real-world automotive dynamic load cycle [19] are simulated: the model is proved to correctly predict the trends of the radical scavenger redistribution.

The work is organized as follows: in Section 2, the experimental methodology is described, with a particular focus on the membrane cerium doping procedure and on the experimental setup and materials used in this work. In Section 3, the 1D in-plane cerium transport model is described, and its calibration and validation are presented. The mechanisms of Ce diffusion, migration under ionic potential gradients and water activity gradients are deeply investigated. In Section 4, the definition of an innovative model framework, based on the coupling between a 1+1D PEMFC performance model and the previously described 1D in-plane cerium transport model, is illustrated and validated on experimental data representative of PEMFC automotive-like operations.

2. Experimental methodology

2.1. Preparation of Ce ion-exchange membranes

EPTFE reinforced membrane prepared with Aquivion ® commercial dispersion (D79-25BS) were provided by Syensqo Specialty Polymers and hereinafter referred to as Aquivion R79. Characterized by an equivalent weight of 790 g/mol_{SO3} and a nominal thickness of 20 μm, they were received in protonated H^+ form. Similarly to the methodology proposed by Baker et al. [2], a doping procedure was developed in order to control the amount of cerium ions absorbed by the membrane. In this work, the cerium content is expressed as loading $\left[mg{\cdot}cm^{-2}\right]$ or ion-exchange fraction f_{Ce}. The latter is the ratio between the actual and the saturation concentration, which is reached when every sulfonic acid group is bound to a cerium cation. It is computed as:

$$C_{Ce,sat} = \frac{MM_{Ce}{\cdot}\rho_{PFSA}}{z_{Ce}{\cdot}EW_{PFSA}};\ f_{Ce} = \frac{C_{Ce}}{C_{Ce,sat}} \tag{1}$$

Where MM_{Ce} is the atomic mass of Ce (140.11 g/mol), ρ_{PFSA} is the density of dry PFSA (1.97 g/cm^3) [2], z_{Ce} is the cerium ion charge (that in this work is equal to 3 since during operation it is assumed that the >99 % of Ce ions exist in the +3 charge state [2,14,25]) and EW_{PFSA} is the equivalent weight of the PFSA (790 g/ $mol_{SO_3^-}$ for the selected membrane). Membranes of size 34 × 10 mm were cation-exchanged by soaking them in aqueous solutions of Ce(III) sulfate for 24h and the desired f_{Ce} was achieved by controlling the concentration of the doping-solution (the absorption curve is reported in the Supplementary Material in Fig. S1). The volume of water in the solution was set to 400 ml while the amount of cerium was changed to achieve the desired Ce ion-exchange fraction, while always ensuring that the total amount of cerium available is sufficiently higher with respect to the amount adsorbed by the sample. Then, the sample was soaked for 1 h in deionized (DI) water to remove excess solution on the surface and dried under ambient conditions. At the two sides of the membrane, Pt/C layers with a loading of 0.1 $mg_{Pt}\ cm^2$ were deposited via Ultrasonic Spray

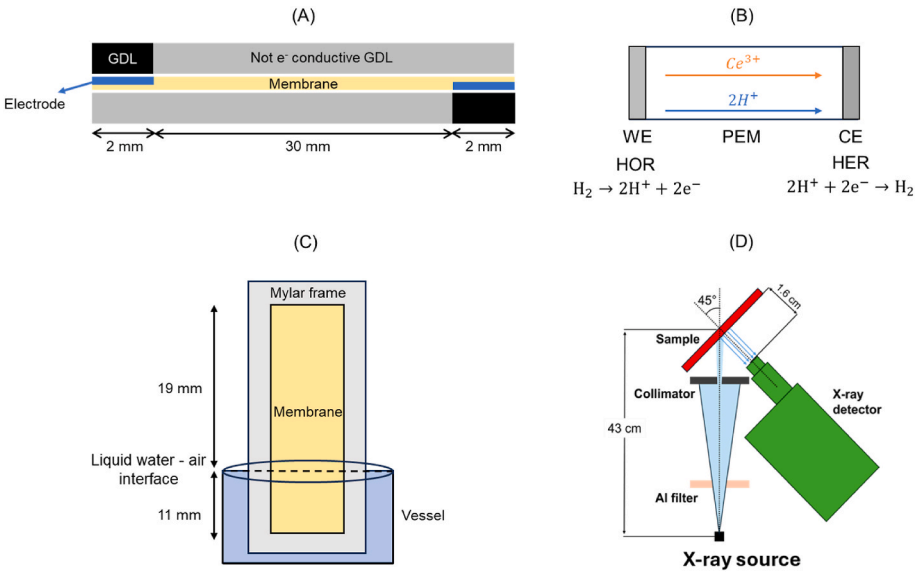

Fig. 1. (A) Cross sectional view of the membrane setup used in the hydrogen pump test performed in this work. Drawing not-in-scale. (B) Schematic of the reactions taking place during the hydrogen pump test. (C) Schematic of the setup used to study the effect of water activity gradient on cerium ion transport: the Ce-ion exchanged membrane is mounted on a Mylar frame and submerged into 700 ml of deionized water. 11 mm of the membranes are in contact with liquid water while the remaining part is exposed to air at 5% RH. Drawing not-in-scale. (D) Schematic of the geometrical setup used to carry out the XRF scans for local cerium quantification. Drawing not-in-scale.

Coating [26]. These two layers were deposited over the whole membrane height (10 mm) and for a width of 2 mm each, at the two opposite sides of the membrane (Fig. 1(A)), and they were necessary to carry out the hydrogen oxidation reaction (HOR) and the hydrogen evolution reaction (HER) in the hydrogen pump tests (Fig. 1(B)).

2.2. Experimental setups

In analogy with what already done in the literature [14,27], hydrogen pump tests were performed to study the in-plane cerium ions migration and diffusion under different operating conditions. The cerium-exchanged Aquivion R79 membranes previously described were assembled in a single-cell Zero-Gradient hardware [28] to ensure homogeneous conditions along the channel (Fig. 1(A)). Two types of GDLs were used at each side of the membrane: a small one (2 × 10 mm) electronic conductive in contact with the catalyst layer (Freudenberg H23 CX653, 250 μm thick) and one not electronic conductive (SAATIfil PES 285/44, 30 × 10 mm, 255 μm thick) in contact with the membrane not covered by the catalyst layer, which prevents the in-plane electronic transport while allowing the gas reactants, flowing into the channels, to properly enter into contact with the membrane hence ensuring the correct hydration state and compression. Finally, rigid gaskets in glass PTFE and in Mylar® were used to prevent gas leakages.

The membrane was conditioned at ambient temperature by supplying overnight a hydrogen flow rate of 0.1 Nl/min at both sides. The hydrogen pump test was carried out at constant temperature, RH and atmospheric pressure with a hydrogen flow rate of 0.3 Nl/min at both working (WE) and counter (CE) electrodes. Heated tubes were used between the bubblers and the hardware, and their temperature was set 10 °C higher than the cell temperature to prevent water condensation. As shown in Fig. 1(B), hydrogen oxidation reaction (HOR) occurs at the working electrode forming protons and electrons which recombine at the counter electrode where hydrogen evolution reaction (HER) takes place. Cerium cations migration is induced from WE to CE, in accordance with the proton flux, by imposing a constant voltage for a fixed amount of time. Afterwards, the membrane is dried out and cooled down with 1 Nl/min of dry nitrogen for 5 min before removal so that cerium back diffusion is hindered. Finally, cerium concentration profile is measured by means of XRF analysis.

Concerning the experimental campaign aimed at understanding the impact of water content on Ce ions transport, described in detail in Section 3.3, the following methodology was adopted and it is shown in Fig. 1(C): the Aquivion R79 membranes, once cerium-exchanged with the same procedure described in Section 2.1, were mounted on a Mylar frame. The frame holding the membrane samples was placed into a vessel containing 700 ml of deionized water at 80 °C such that the lower part of the membrane was submerged while the remaining part was above the liquid-air interface, where the temperature was set at 80 °C with 5% RH. To control the operating conditions throughout the duration of the test, a temperature-controlled chamber (BINDER KT53 [29]) was used. To avoid water droplet condensation on the part of the membrane above the liquid-air interface, a custom Mylar frame was designed. During the experiment, the water level was visually monitored to maintain the submerged condition. The test lasted 24 h, after which the in-plane cerium loading profile was quantified using the XRF setup described in the next section.

2.3. X-ray fluorescence analysis of cerium distribution

The areal concentration profiles of cerium along the membrane length were measured using an in-house X-ray fluorescence system called RETINA (Fig. S2(A)). The RETINA facility employed a high-power, tungsten anode X-ray tube operating at 70 kVp and 2.30 mA with a 0.6 mm focal spot size. The low-energy cutoff of the X-ray source spectrum was around 15 keV.

Characteristic X-ray spectra were acquired using a Peltier-cooled CdZnTe detector (XR-100T-CZT, Amptek Inc.) providing 400 eV FWHM energy resolution at the Fe Kα line. A custom collimator restricted the X-ray beam to 1 mm width on the scanning axis and a 5 mm height (on the membrane surface), achieving spatial resolution sufficient for mapping the local cerium distribution. This X-ray beam dimension on the membrane was confirmed through a CCD-based X-ray imaging detector. The membrane scan was done by moving the sample on 2 axes with a motorized stage (from THORLABS) fixed on an optical table. A 1.6 cm sample-detector-distance was maintained during the scans (Fig. 1(D)).

Elemental quantification employed the fundamental parameters method using a standard reference material, with PyMca software [30].

System calibration was performed by irradiating a thin 6-element XRF reference standard from AXO Dresden GmbH. To exploit the enhanced performance of the CdZnTe detector in the few tens of keV energy range, Ce Kα and Kβ fluorescence lines at 34 and 39 keV were selected for quantitative analysis.

All XRF spectra underwent batch processing in PyMca using the Single Layer strategy with corrections for secondary excitations. The membrane was modelled with a PTFE base material adopting the density equal to 2 g/cm^3 and thickness equal to 20 μm. Background subtraction employed the SNIP (Sensitive Nonlinear Iterative Peak-clipping) algorithm [31] to account for contributions from Compton scattering continuum and low-frequency detector noise (Fig. S2(B)). Relative uncertainties were estimated to be equal to the net peak area uncertainties provided by PyMca. Other sources of uncertainties like detection efficiency and geometric setups were minimized through the system calibration process in the same energy range of the emitted X-rays from the sample.

2.4. X-ray tomography analysis

X-ray tomography of pristine and aged samples was performed using a TESCAN UniTOM HR system [32], designed for high-resolution, multiscale imaging. The system supports continuous rotation (for the 4DCT), in situ experiments, and the maximum achievable resolution is 600 nm. The X-ray source operates between 30 and 160 kV, with multiple detectors available for different samples. Volume reconstruction was carried out using Panthera, the TESCAN dedicated software for 3D/4D CT analysis.

In this study, three scans were acquired on a pristine and the aged sample of the commercial catalyst coated membrane tested for 330 operating hours of the high power protocol, later reported: a multiscale imaging of both air inlet and air outlet regions of the cell was carried out to identify possible heterogeneities in the morphological structure. Scans were performed at 100 kV, with a voxel size of 2.05 μm and an approximate field of view (FOV) of 3 × 3 mm on the sample. The parameters were chosen as a trade-off between achieving sufficient spatial resolution and maintaining a field of view large enough to capture representative morphological features of the catalyst layers and of the membrane. The Panthera software was used for post-processing analyses.

3. In-plane cerium transport model

3.1. Model formulation

Cerium transport is affected by three components [14]: (i) the ionic potential gradient ($\nabla\Phi_{ionic}$), (ii) the back diffusion of Ce ions due to the resulting concentration gradient (∇C_{Ce}) and, as recently reported in the literature [5,16,27,33], (iii) the water activity gradients, with a movement from high humidity to low humidity. Therefore, to account for all these mechanisms, the 1D in-plane transport of Ce ions is modelled according to the Nernst-Planck equation which, in its more general form, is expressed as:

$$\varepsilon_{ion}\frac{\partial C_{Ce}}{\partial t} = \nabla\cdot\left[D_{Ce}\cdot\varepsilon_{ion}^{1.5}\cdot\nabla C_{Ce} + u_{Ce}\cdot\varepsilon_{ion}^{1.5}\cdot C_{Ce}\cdot\nabla\Phi_{ionic} + \xi_{Ce}\cdot D_{Ce}\cdot C_{Ce}\cdot\varepsilon_{ion}^{1.5}\cdot\nabla\ln a_w\right] \quad (2)$$

Where C_{Ce} is the cerium ion concentration and ∇C_{Ce} is the concentration gradient, $\nabla\Phi_{ionic}$ is the ionic potential gradient, D_{Ce} is the diffusion coefficient, u_{Ce} is the migration coefficient and ξ_{Ce} represents the electro-osmotic drag coefficient. It is worth noting that the coefficients D_{Ce}, u_{Ce} and ξ_{Ce} are all corrected for the Bruggeman correction, $\varepsilon_{ion}^{1.5}$, to account for the reduced mobility in the case of an actual ionomer fraction ε_{ion} lower than 1, as in the catalyst layer.

To be solved, Equation (2) requires specific boundary conditions, i.e. null Ce flux at the left and right boundaries of the computational domain:

$$\vec{n}\cdot\left(-D_{Ce}\cdot\varepsilon_{ion}^{1.5}\cdot\nabla C_{Ce} - u_{Ce}\cdot\varepsilon_{ion}^{1.5}\cdot C_{Ce}\cdot\nabla\Phi_{ionic} - \xi_{Ce}\cdot D_{Ce}\cdot C_{Ce}\cdot\varepsilon_{ion}^{1.5}\cdot\nabla\ln a_w\right) = 0 \quad (3)$$

Table 1
Ce diffusion properties and corrective factors for water content and protonic conductivity adopted in the model used in this work.

Property	[Units]	Equation	Reference
D_{Ce}	$[cm^2/s]$	$\frac{1.3\cdot10^{-18}\cdot exp(0.07831\cdot T)}{1+\exp(-0.6163^*(\lambda-8.248))}$	[12,27] (NR 211)
D_{Ce}	$[cm^2/s]$	$\frac{6.6\cdot10^{-19}\cdot exp(0.07831\cdot T)}{1+\exp(-0.6163^*(\lambda-8.248))}$	[14] (Nafion XL)
CF_λ	[−]	$0.2359\cdot\exp(-(2.266\cdot10^{-16}\cdot\exp(37.34\cdot RH)+0.08093\cdot\exp(2.675\cdot RH))\cdot f_{Ce})+0.76$	[2]
λ	[−]	$\lambda_0\cdot CF_\lambda$	–
λ_0	[−]	Nafion XL: $12.48\cdot RH^3-14.25\cdot RH^2+10.2\cdot RH+0.01$	[39]
		Aquivion R79: $1.371\cdot10^{-5}\cdot RH^3-0.0014\cdot RH^2+0.092\cdot RH+0.24$	From dynamic vapor sorption measurements
Φ_{CC}	[−]	$\Phi_W\cdot\left[(1-f_{Ce})+\frac{f_{Ce}}{3}\right]$	[2]
Φ_W	[−]	$\frac{\lambda}{\lambda+\overline{V_P}/\overline{V_W}}$ $\overline{V_P}=\frac{EW_{PFSA}}{\rho_{PFSA}}=558\ cm^3/mol$ $\overline{V_W}=18.1\ cm^3/mol$	[2]
CF_σ	[−]	$e^{-b(\lambda)\cdot fce}$	[2]
b	[−]	Nafion XL: $12.5281\cdot e^{-0.2658\cdot\lambda}$	Fitted from Ref. [2] and corrected to account for Nafion XL sorption isotherm
		Aquivion R79: $11.691\cdot e^{-0.2416\cdot\lambda}$	Fitted from Ref. [2] and corrected to account for Aquivion R79 sorption isotherm
σ	$[S/m]$	$\sigma_0\cdot CF_\sigma$	–

The diffusion coefficient D_{Ce}, whose expression is reported in Table 1 and that is graphically shown in Fig. 2(A), increases with temperature and water content, showing an asymptote for values of water content larger or equal to the equilibrium with liquid water (i.e. RH equal to 100 %). Indeed, as suggested by Ref. [12], at a given temperature the rates of cation diffusion are the same whatever the membrane is saturated with liquid water or water vapor. It can be noted that the diffusion coefficient for cerium ion in a Nafion XL (represented in yellow in Fig. 2(A)) is half than the one in a NR211 membrane (represented in red in Fig. 2(A)) at same temperature (80 °C) and water content. This may be attributed to the presence of the mechanical reinforcement and/or different ionomer properties (e.g., membrane thickness) as already suggested in literature [2,16]. The diffusion coefficient adopted in this work is coherent with Nafion XL data since it leads to a better adherence to our experimental results.

Concerning the migration coefficient in Equation (2), u_{Ce}, a brief clarification is needed. The migration behaviour of Ce ions in PFSA membranes may not strictly follow the migration theory of free cations in dilute solutions [34]. The expression of u_{Ce} was previously discussed in the literature: Baker et al. [14,27], for instance, compared the migration coefficient calculated using the Einstein relation with the value computed applying the Okada Theory [35] and estimated through the model by fitting the Ce migration profiles obtained in different operating conditions on a Nafion XL membrane. Their sensitivity analysis showed that the three different methods yield values of the same order of magnitude in various operating conditions tested. For this

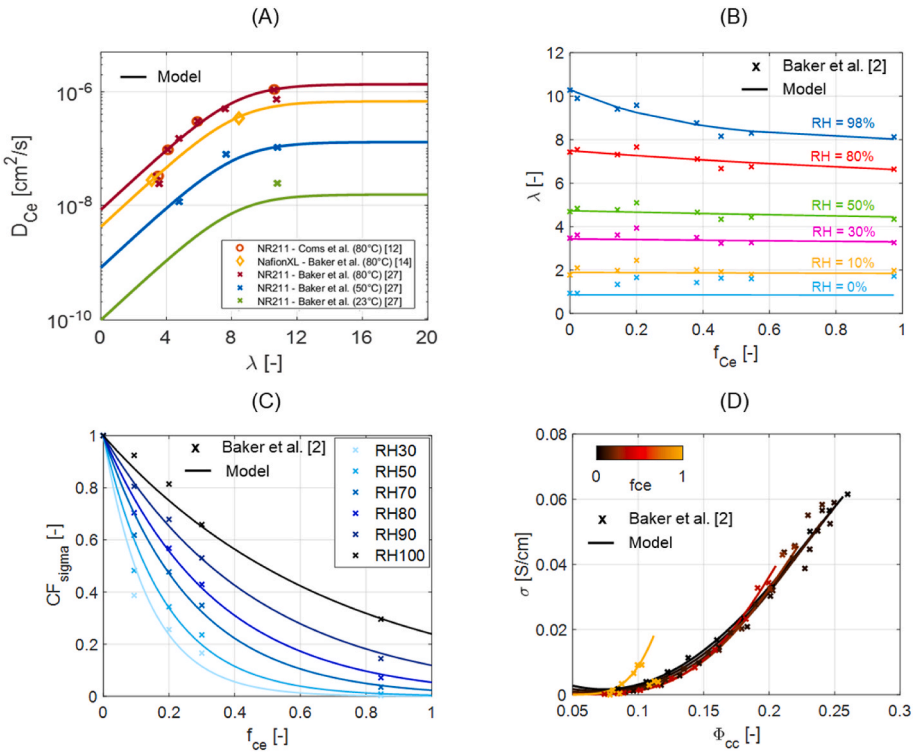

Fig. 2. (A) Ce diffusion coefficient expressed as a function of water content and temperature. Comparison between the correlation adopted in this work and the experimental data taken from the literature [12,14,27]. (B) Water uptake behaviour for different RHs and cerium ion-exchange fractions. Comparison between experimental data taken from Ref. [2] and correlation adopted in this work. (C) Protonic conductivity correction expressed as a function of f_{Ce} for different RH values. Comparison between experimental data taken from Ref. [2] and correlation adopted in this work. (D) Protonic conductivity as a function of hydrated charge carrier network volume fraction for different Ce ion-exchange fractions. Comparison between experimental data taken from Ref. [2] and correlation adopted in this work.

reason, and to reduce the number of calibrated parameters, in this work we decided to adopt the Einstein relation reported in Equation (4):

$$u_{Ce} = \frac{z_{Ce} D_{Ce} F}{RT} \tag{4}$$

Where z_{Ce} is the charge number, considered equal to 3, F is the Faraday constant, R is the ideal gas constant, T is the temperature in Kelvin and D_{Ce} is the diffusion coefficient previously described.

Concerning the effect of water activity gradients on cerium movement, it must be specified that, to the best of the authors' knowledge, in the literature the information provided is very limited, and the modelling of this mechanism is still challenging. Cerium ion transport driven by water activity gradient in the in-plane direction is currently under discussion and both the exact mechanism and the intensity/time-scale of this phenomenon are still unclear [5,8]. As far as concerns experimental data, Morita et al. [33] studied the in-plane cerium ions transport due to RH gradient by feeding one side of the cell with nitrogen at 90 % RH and the other side of the cell with nitrogen at 50 % RH. Under such conditions they observed that Ce ions movement took about 90 min on a 5 mm scale. In this work, it was decided to adopt the same modelling approach recently proposed by Shinozaki et al. [16], who derived the last term of the previously presented Equation (2) from the Onsager reciprocal relations for gradients in the chemical potentials of cations and water, while the interaction between protons and cations was neglected according to the works [16,36]. While, as told, ξ_{Ce} represents the electro-osmotic drag coefficient, a_w is the water activity which we assumed equivalent to the relative humidity. To study the time scale of this phenomenon and to provide a reasonable value for ξ_{Ce}, both *ad hoc* tests carried out in this work and literature data [16] have been considered, as largely discussed in Section 3.3.

If, on the one hand, the introduction of Ce ions as radical scavenger is fundamental to mitigate the chemical degradation of the PEM and, therefore, enhance PEMFC lifetime, on the other hand it may negatively affect the structure-transport relationship of the polymer [2]. Indeed, as stated in the literature, the ionomer water uptake [2,35], especially at high Ce ion-exchange fraction f_{Ce} and at high relative humidity, is one of the membrane properties most affected by the presence of Ce ions. This effect is included in this work by correcting the water sorption isotherm of the membrane in protonated form (i.e. in the absence of cerium ions) for a corrective factor, CF_λ, properly calibrated on experimental data available in the literature [2] and accounting for the effect of both Ce ion-exchange fraction and RH according to the formulation reported in Table 1 and shown in Fig. 2(B).

Membrane conductivity, σ, depends on the operating conditions, i.e. temperature and water content. However, it is also strongly affected by the Ce ion-exchange fraction [2,8,37,38]. Therefore, based on the experimental data available by Baker et al. [2], a corrective factor for the protonic conductivity was fitted as a function of the Ce ion-exchange fraction and of the water content (see Fig. 2(C) and (D)). As reported in Ref. [2], it is worth noting that the weight of this corrective factor increases, i.e. the protonic conductivity decreases, as f_{Ce} increases and the water content decreases (or, equivalently, the RH decreases). This behaviour may be explained by (i) the reduced Ce ions mobility at low water contents, which means that the interaction between protons and the sulfonic acid groups of the PFSA membranes is hindered and by (ii) the reduction of mobile water for protons to move through due to the stronger bond between Ce ions and the sulfonic acid groups [2]. To take into account all these aspects, the actual conductivity σ is computed multiplying the protonic conductivity of the membrane in protonated form, σ_0, by the corrective factor, CF_σ, whose expression is reported in Table 1. The corrective factor CF_σ was calibrated from Ref. [2], where the conductivity of a Nafion NR211 membrane was expressed as a function of the hydrated charge carrier network volume fraction, Φ_{CC} (see Table 1), and it accounts for both the effect of Ce ion-exchange

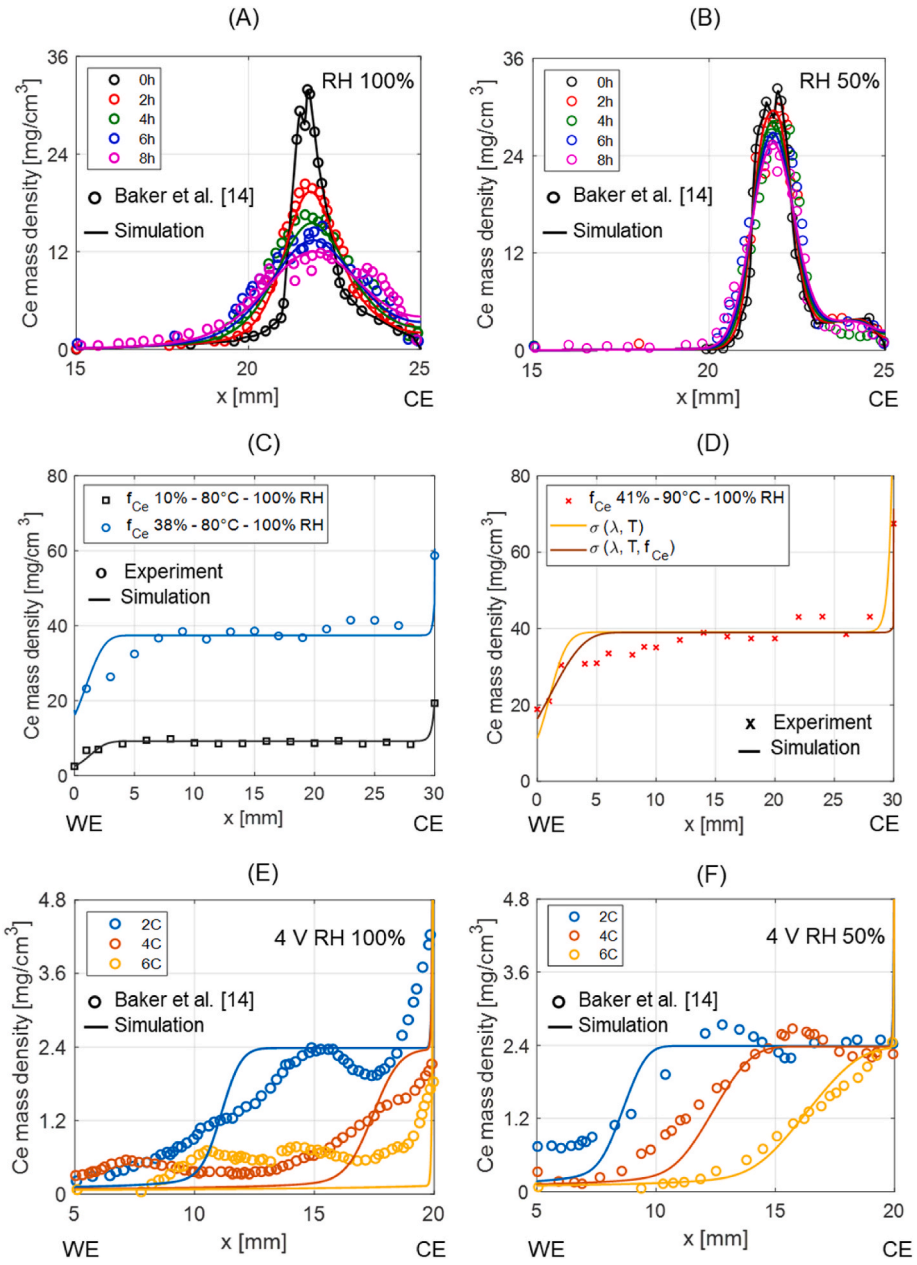

Fig. 3. Comparison of Ce ions diffusion and migration profiles between experimental data (symbols) and model simulations (solid lines). WE stands for working electrode while CE stands for counter electrode. Ce ions diffusion at 80 °C and 100% RH (A) and at 80 °C and 50% RH (B) in a Nafion XL membrane at different operating times. Experimental data taken from Ref. [14]. (C) This work migration profile in Aquivion R79 membranes at 1V, 80 °C and 100% RH for two different initial Ce contents. (D) This work migration profile in Aquivion R79 membranes at 1V, 90 °C and 100% RH with and without dependence of protonic conductivity from local f_{Ce}. (E) Migration profile in Nafion XL membranes after 2C, 4C and 6C charge transfer at 4V, 80 °C and 100% RH (E) and 50% RH (F). Experimental data taken from Ref. [14].

fraction and RH. However, as it will be better explained in the next section, the 1D in-plane cerium transport model just described will be validated on experimental data gathered via hydrogen pump tests on both Nafion XL and Aquivion R79 membranes, which have vapor sorption isotherms different from those of Nafion NR211. Therefore, to express CF_σ as a function of water content rather than RH, the sorption isotherms of the different membranes were used to correlate λ to RH. This is why, in Table 1, the dependence of CF_σ on λ varies from one membrane to the other.

3.2. Model validation on diffusion and migration data

In analogy with the literature, the 1D in-plane cerium transport model, described and calibrated in the previous section, is now validated on a wide set of experimental data gathered by hydrogen pump operation. The tests reported in this section highlight the role of both Ce diffusivity and ionic potential gradient, by taking into consideration the combined diffusion and migration processes. Indeed, it is worth noting that, since no water content gradient arises during the hydrogen pump test [14], the Nernst-Planck equation described by Equation (2) reduces to Equation (5):

$$\varepsilon_{ion}\frac{\partial C_{Ce}}{\partial t} = \nabla\cdot\left[D_{Ce}\cdot\varepsilon_{ion}^{1,5}\cdot\nabla C_{Ce} + u_{Ce}\cdot\varepsilon_{ion}^{1,5}\cdot C_{Ce}\cdot\nabla\Phi_{ionic}\right] \quad (5)$$

Where the ionomer fraction ε_{ion} is set to 1 since only the membrane domain is considered.

Table 2
Operating conditions of the hydrogen pump test used to validate the in-plane migration/diffusion Cerium transport model. The data referred to Nafion XL membrane are taken from Ref. [14] while those related to Aquivion R79 membrane are gathered in house by the experimental protocol described in Section 2.2.

Membrane	RH [%]	T [°C]	f_{Ce} [%]	Voltage [V]	Average Current [A]	Proton conductivity σ_0 [S/m]	Charge transferred Q [C]	Ref.
Nafion XL	100	80	3	4	$2.82 \cdot 10^{-4}$	10	2 - 4 - 6	[14]
Nafion XL	50	80	3	4	$3.96 \cdot 10^{-5}$	1.5	2 - 4 - 6	[14]
Aquivion R79	100	80	10	1	$1.04 \cdot 10^{-4}$	14.6	1.5	This work
Aquivion R79	100	80	38	1	$3.35 \cdot 10^{-5}$	4.7	0.5	This work
Aquivion R79	100	90	41	1	$8.69 \cdot 10^{-5}$	5.2	0.5	This work

To apply the 1D in-plane cerium transport model it is, first of all, necessary to understand whether the expression adopted in this work for the diffusion coefficient, D_{Ce}, is correct. For this purpose, experimental data available in the literature [14] and representative of cerium diffusion only (i.e. in absence of any potential applied) are used. The initial (0 h) cerium profiles experimentally obtained by Baker et al. are shown in Fig. 3(A) and (B). The large concentration gradient induces back diffusion of cerium ions over time. By comparing model simulations with the XRF quantification carried out every 2 h, it is possible to appreciate the good adherence between model simulations and experimental data at 80 °C, both at 100% RH and 50% RH: in particular, it is worth noting the ability of the model to correctly predict the much lower diffusion occurring at lower relative humidity.

In addition, the combined migration/diffusion model was validated using data collected during hydrogen pump operation under potential gradients. These tests were conducted on various PFSA membranes with different f_{Ce} and operating conditions, such as relative humidity, temperature, and applied potential gradient, as summarized in Table 2. Concerning the experimental data referred to Nafion XL membrane [14], different migration profiles - representative of different charge transferred (Q) from the working to the counter electrode - are considered and compared with model simulations. Concerning our data on Aquivion R79 membranes instead, the migration profiles obtained at end of the test, i.e. after 4 h, are compared with model simulations. The charges transferred, expressed in coulombs, are listed in Table 2 for all the tests.

As it is reported in Fig. S3(A), it is worth noting that for the Aquivion R79 membrane used in this work, although the applied potential gradient was kept constant to 1 V throughout the duration of the test, the resulting current density progressively decreases with time due to a gradually cerium accumulation towards the counter electrode. Moreover, depending on the cerium doping level, also the proton conductivity changes locally along the membrane length and, hence, varies with the testing time. Therefore, given a constant applied potential gradient, in the simulations the proton conductivity was properly changed by solving the ionic charge conservation to compensate for the progressive decrease of the current density in time. The current and ionic potential profiles used in the model are shown in the Supplementary Material (Fig. S3(B)–(C)).

The model validation on experimental data representative of hydrogen pump operation is shown in Fig. 3. As it can be appreciated from Fig. 3(C), at fixed temperature and RH, a reduction in the initial f_{Ce} gives rise to a flatter migration profile, which can be attributed to a lower contribution of the migrative flux which is proportional to cerium concentration $\left(u_{Ce} \cdot \varepsilon_{ion}^{1,5} \cdot C_{Ce} \cdot \nabla \Phi_{ionic}\right)$. Moreover, analysing the case with an initial cerium doping level equal to 38% (blue line in Fig. 3(C)), we can also observe a difference in the transitions towards both the electrodes: because of a lower cerium content, the transition occurring close to the WE is always less steep than the one occurring at the CE. This aspect, which can be appreciated also from the data taken from the literature [14] in Fig. 3(E) and (F), is captured by the model and will be more detailed later. Fig. 3(D) shows the effect of temperature on Ce mobility: an increase in the operating temperature, coupled with a slightly higher initial Ce concentration, determines a faster transport of cations from the working towards the counter electrode at fixed applied potential and RH, which is a relevant aspect for heavy-duty operating conditions that, because of higher loads, can be characterized by much higher working temperatures [1,40]. In Fig. 3(D), it is also shown the effect that the correction of protonic conductivity for the local Ce ion-exchange fraction has on the migration profile. As already discussed in the previous section, f_{Ce} strongly affects the protonic conductivity. In particular, at fixed temperature and water content, the protonic conductivity decreases as f_{Ce} increases (Table 1). Therefore, during the hydrogen pumping procedure, due to the cerium redistribution, we expect the local protonic conductivity to vary along the x-coordinate. In particular, near the counter electrode, the elevated f_{Ce} results in a lower σ. Thus, being the ionic potential expressed as $-\frac{i}{\sigma}$, where i is the experimentally measured current density and σ is the protonic conductivity, the local ionic potential gradient will be higher close to the counter electrode rather than at the working one. The impact is visible in Fig. 3(D), where the yellow line represents the outcome without the local dependence of proton conductivity on Ce content, while the red curve includes this phenomenon description. The introduction of this correction on the protonic conductivity helps to explain the different steepness of the two transitions and the fact that, according to both experiments and model simulations, the fastest occurs closer to the counter electrode.

Fig. 3(E) and (F) show the validation of the proposed model on data taken from the literature [14], and representative of different RH conditions. As it can be appreciated, according to both experiments and simulations, and coherently with previous works [12,14], cerium mobility is strongly hindered at low water contents. Indeed, at the same applied potential and amount of exchanged charge, Ce transport proceeds more slowly at 50% RH. This is particularly evident for the cases 4C and 6C: at 100% RH, Ce ions are completely depleted from the working electrode while, a 50% RH, the depletion zone is significantly reduced.

To summarize, the results shown in this section prove the capability of the in-plane transport model to correctly predict cerium migration under a wide range of RHs, applied potentials and initial Ce ion-exchange fractions. Despite the good adherence between model simulations and experiments, some discrepancies are still present, especially looking at the transition occurring close to the working electrode which occurs faster according to the simulations. This small discrepancy with respect to all the experiments may be attributed to the Einstein relation used to model the migration coefficient: indeed, as reported in Ref. [14], the Einstein relation, as the Okada theory [35], might lead to an overestimation of the mobility coefficient u_{Ce} and, therefore, of Ce ions transport. To better investigate the impact of the migration coefficient on hydrogen pump transport profiles, a sensitivity analysis on the value assumed by u_{Ce} has been carried out, and it is reported in Fig. S4. With the model parametrization adopted in this work, the Einstein relation allows to maximize the adherence between simulations and experiments. Anyway, according to the evidences reported in the literature by Baker et al. [14] and Shinozaki et al. [16], the migration coefficient computed by the Einstein relation could vary, being reduced by a factor 1.5 and 3 respectively. As it can be appreciated by the results of this analysis, a reduction of this parameter simply determines a horizontal shift of the f_{Ce} profile, without affecting the steepness of the transition occurring close to the WE. Therefore, the adopted approach was considered accurate enough for the purpose of this work, even though

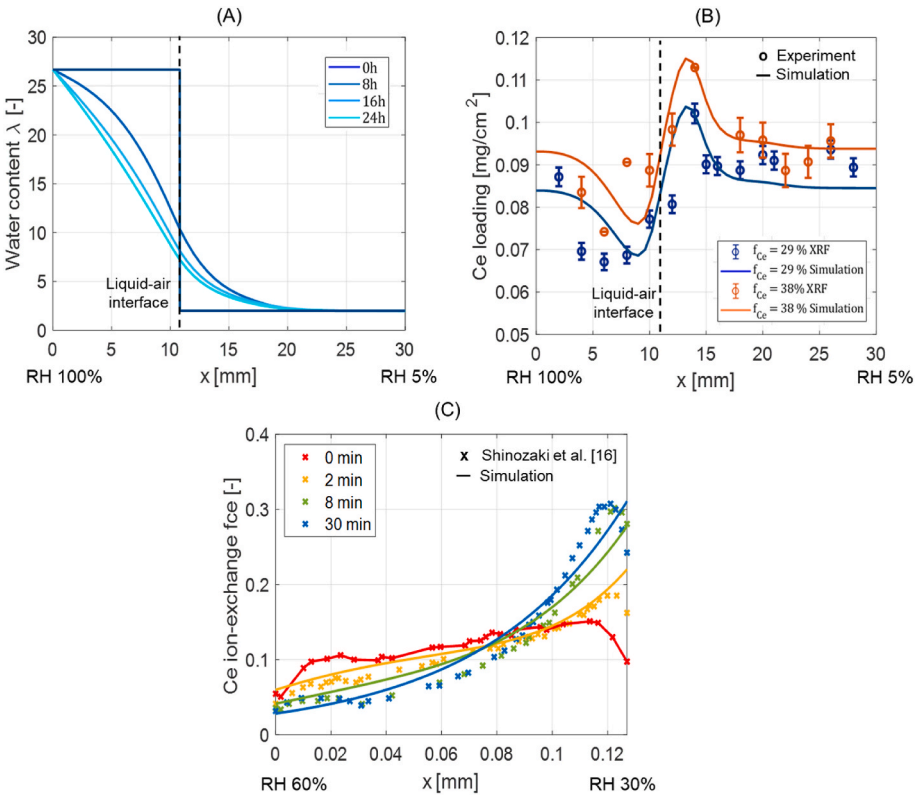

Fig. 4. (A) Water transport across the membrane at different time according to the simulations. (B) Comparison between model simulations and experimentally measured profiles for the samples with an initial Ce ion-exchange fraction equal to 29% and 38%. The electro-osmotic drag coefficient, ξ_{Ce}, was calibrated to minimize the RMSE. (C) Comparison between model simulations and experimental data taken from Ref. [16] and representative of through-plane Ce transport due to RH gradient.

future investigations regarding more complex and complete descriptions could help to further explain the small discrepancies still present between simulations and experiments.

3.3. Impact of relative humidity gradient on cerium ion transport

The effect of water activity (i.e. relative humidity) gradient on cerium ions transport, as it was previously discussed, is currently under investigation in the literature and both the mechanism and the timescale of the phenomena are not well known. Baker et al. [5] suggest that the presence of a water content gradient gives rise to a water flux from the high RH regions to the low RH regions which, in turn, by convection, drags Ce ions with it. Ehlinger et al. [8] talk about a solvent-ion interaction between Ce cations and water: Ce ions in water become hydrated, meaning they attract and coordinate a shell of water molecules. Therefore, to quantify the impact of this driving force on cerium ions transport, *ad hoc* tests were carried out in this work, according to the methodology previously shown in Fig. 1(C). Two different membrane samples, with an initial Ce ion-exchange fraction equal to 29% and 38%, respectively, were tested under a 100%–5% RH gradient. The choice to adopt an extreme gradient of 100% - 5RH% was made to exacerbate the driving force responsible for cerium transport and, therefore, to obtain a valuable radical scavenger movement in a desired limited amount of time, without compromising the accuracy of the experiment.

The resulting migration profile for the two samples are shown in Fig. 4(A), where the bars indicate the error associated with the XRF quantification. As it can be appreciated from Fig. 4(A), for the sample with f_{Ce} equal to 29%, cerium ions take about 24 h to be transported on a 12 mm scale: indeed, with respect to the initial condition, in which the cerium content was homogeneous across the whole membrane length, at the end of the test the cerium loading decreases at the high RH side and progressively increases moving towards the low RH side, achieving its maximum at the x-coordinate equal to 12 mm. Then, going further towards the end of the membrane, the cerium loading decreases again and stabilizes around the initial content, meaning that in the low RH region (i.e. far from the submerged portion of membrane) the cerium ions transport is strongly hindered. This behaviour, that is coherent with what already observed by Morita et al. [33], may be explained by the fact that, in the low RH region, the water content and thus the diffusion coefficient are very low, further contributing to slow down cerium ions transport.

The same trend can also be observed for the case with an initial f_{Ce} equal to 38%, even though in this case, under the same RH gradient, the transport length increases to 15 mm after 24 h. Indeed, being the transport rate due to relative humidity gradient proportional to Ce ions concentration (Equation (2)), it is reasonable that cerium transport is speeded up as the initial content increases. Anyway, in both the two cases it is worth noting that an in-plane Ce transport towards the low humidity side occurs, coherently with what already observed in the literature [5,16,33,41].

To identify and propose a reasonable range of values for the coefficient ξ_{Ce} in Equation (2), the 1D in-plane cerium transport model described in Section 3.1 was used under the assumption that, since no ionic potential gradient is applied, only the contributions given by the concentration and RH gradients are considered:

$$\varepsilon_{ion}\frac{\partial C_{Ce}}{\partial t} = \nabla\cdot\left[D_{Ce}\cdot\varepsilon_{ion}^{1,5}\cdot\nabla C_{Ce} + \xi_{Ce}\cdot D_{Ce}\cdot C_{Ce}\cdot\varepsilon_{ion}^{1,5}\cdot\nabla\ln RH\right] \quad (6)$$

To be applied, Equation (6) requires the knowledge of the RH gradient. As already explained in the experimental methodology for the test under analysis, the lower part of the membrane is in contact with liquid water, while the upper part is exposed to air. Therefore, a water transport from the high RH side towards the low RH side takes place. As a consequence, to determine the cerium migration profile from a

Table 3
Water transport model parameters.

Property	[Units]	Equation	Reference
D_λ	$[m^2/s]$	$\left(1+\frac{1.8\cdot10^{-5}}{EW/\rho_{ion}}\lambda\right)^{-2}\cdot0.054\cdot(1.0+2.7e^{-3}\lambda^2)\left[1+tanh\left(\frac{\lambda-2.62}{0.88}\right)\right]exp\left(-\frac{27800}{\mathscr{R}T}\right)$	[42,43]
S_λ	$[1/s]$	$-k_g\frac{P}{A}\cdot\left(\lambda-\lambda^*_{eq}\right)$	[24]
k_g	$[m/s]$	$6.8\times10^{-6}\cdot\lambda^{1.6}\cdot exp\left(\frac{20000}{R}\cdot\left(\frac{1}{303.15}-\frac{1}{T}\right)\right)$	[44]
$S_{M/air}$	$[mol/m^2/s]$	$h_{air}\cdot\left(C_v-C_v^{M/air}\right)$	[45]
h_{air}	$[m/s]$	$2\cdot10^{-3}$	[45]
P	$[m]$	$2\cdot10^{-2}$	Geometry
A	$[m^2]$	$2\cdot10^{-7}$	Geometry
λ_{eq}	$[-]$	$(1-\tanh(10\cdot s))\cdot(0.3+7\cdot RH\cdot(1-\tanh(RH-0.5)))+0.69\cdot(12.2-3.52)\cdot\sqrt{RH}\cdot\left(1+\tanh\left(\frac{RH-0.92}{0.23}\right)\right)+\tanh(10\cdot s)\cdot(12.2+0.181\cdot(T-273.15))$	[24,45,46]
λ_{MAX}	$[-]$	27	Calculated
λ_{MIN}	$[-]$	2	Calculated

modelling point of view, it t is necessary to couple Equation (6) with Equation (7), which describes the water transport inside the ionomer due to the diffusion mechanism:

$$\frac{\partial}{\partial t}\left(\frac{\rho_{ion}}{EW}\lambda\right)=\nabla\cdot\left(D_\lambda\frac{\rho_{ion}}{EW}\cdot\nabla\lambda\right)+S_\lambda \tag{7}$$

Where D_λ is the dissolved water diffusivity, which depends on temperature and water content according to Refs. [42,43], and S_λ is the source term, that accounts for water transport at the ionomer/gas boundary interface. The complete formulation of D_λ and S_λ terms is listed in Table 3, where the interfacial mass transport coefficient, k_g, depends on temperature and water content [44]. The equilibrium water content in the source term, λ^*_{eq}, is computed ensuring that in the region of the membrane exposed to air the source term S_λ is equal to the convective water flux at the membrane-air interface, $S_{M/air}$, which depends on the convective mass transfer coefficient h_{air}, on the vapor concentration at the membrane/air interface, $C_v^{M/air}$, function of the RH of the surrounding air, and on the vapor concentration at the membrane surface, C_v, function of the equilibrium water content [45].

The evolution of water content λ in the in-plane x direction is shown in Fig. 4(A) for different time steps of the simulation. At time zero the water content is equal to λ_{MAX} in the region of the membrane in contact with liquid water and equal to λ_{MIN} in the region of the membrane exposed to air which, for modelling purposes, is set equal to 2 [47]. The value of λ_{MAX}, listed in Tables 3, is computed from the sorption isotherm curve λ_{eq} reported in Table 3 for temperature equal to 80 °C, RH equal to 100% and liquid water saturation, *s*, equal to 1. Starting from this initial condition, the water balance is solved along the in-plane direction of the membrane: as shown in Fig. 4(A), a progressive water transport occurs from the high humidity towards the low relative humidity side. Knowing the water content profile, it is possible to determine the RH gradient across the membrane which, if provided as an input to the cerium transport model described by Equation (6), allows to simulate the loading profiles shown in Fig. 4(B): the coefficient ξ_{Ce} affecting cerium transport due to RH gradient was calibrated. In particular, the value equal to 3.5 was found to minimize the root mean square error between simulations and experiments, as confirmed by Fig. S5(A)–(B), where a comparison between model simulations and experiments is shown for values of ξ_{Ce} ranging between 1 and 7. As it can be appreciated from the Supplementary Material, a variation of the electro-osmotic drag coefficient affects the intensity of cerium depletion in the high humidity side of the membrane and cerium accumulation close to the liquid water/air interface, while the shape of the cerium transport profile is unaltered. Indeed, as ξ_{Ce} decreases, both the downward and upwards Ce loading peaks increase in absolute value, but their location remains unaffected. To prove the goodness of the value found for the electro-osmotic drag coefficient, the experimental data taken from Ref. [16] were also simulated. These data are representative of cerium transport profiles in the through-plane direction when a difference in terms of RH is applied at the anode and the cathode side of a CCM (i.e. RH equal to 60% and 30%, respectively). As it can be appreciated from Fig. 4(C) and from Fig. S5(C), a progressive cerium transport towards the low relative humidity side occurs with time and the intensity of such phenomenon is regulated by the electro-osmotic drag coefficient. The model simulations are able to capture the cerium ion-exchange profiles at different times of the experiment by using the parametrization described in Section 3.1 and setting ξ_{Ce} equal to 3.5, as calibrated before. Therefore, an electro-osmotic drag coefficient $\xi_{Ce}=3.5$ is considered sufficiently accurate and it will be also used in the following analysis. An additional sensitivity analysis for this coefficient will be carried out in Section 4.6.

4. Coupling between 1+1D dynamic PEMFC performance model and the 1D in-plane cerium transport model

4.1. Dynamic load cycle protocols and model framework definition

The real-world automotive driving cycle DLC consists in the ID-FAST single cell protocol extensively described in our previous works [9,19,24] and here briefly summarized. The complete driving cycle is composed of a low-power (LP) and a high-power (HP) operating mode, separated by a short-stop procedure. The LP protocol, during which the current density ranges among 0.095 A cm^{-2} and 0.59 A cm^{-2}, lasts 40 min and it is followed by a 5 min short-stop. During this operating mode, cell temperature and reactant pressures are kept constant, respectively to 71 °C and 140 kPa and 190 kPa for cathode and anode side. Relative humidity at cathode and anode channel inlet is set to 30% and 50% respectively (Fig. 5(B)). The HP mode is characterized by current densities ranging among 0.095 A cm^{-2} and 1.75 A cm^{-2}; it lasts 20 min and, once again, it ends with a 5 min short-stop. During this operating mode, a ramp increases the cell temperature from 71 °C to 90 °C, while the dew point is switched from 58 °C to 72 °C at the anode, and from 43 °C to 57 °C at the cathode [19,24,48]. Stoichiometry is set constant to 1.4/1.6 for anode and cathode respectively. In this work, the effects of both the operating modes and of the complete DLC protocol on Ce redistribution are investigated. The complete driving cycle is repeated for 1000 h, while for the single LP and HP modes 400 h and 330 h are considered respectively.

In-plane cerium distribution is studied on a commercial catalyst coated membranes (CCM). As reported in previous studies [9,19,24], it is characterized by anode/cathode catalyst layers of 0.1/0.5 $mg_{Pt}cm^{-2}$ separated by a membrane whose thickness is 18 μm. The membrane includes a mechanical reinforcement and cerium as radical scavenger. By means of an X-ray fluorescence analysis, it was possible to determine the cerium concentration for the pristine CCM: considering a saturation concentration equal to 90.2 $mg_{Ce}cm^{-3}$ [2], the initial cerium content f_{Ce} was calculated to be around 5.5% [9]. The cell consists of a 25 cm^2 segmented hardware [19,49,50] whose graphite flow plates, as shown in Fig. S6(B), are segmented into four portions of non-uniform active area: segment 1 = 5.83 cm^2, segment 2 = 5.80 cm^2, segment 3 = 7.65 cm^2 and segment 4 = 5.72 cm^2. The cell adopts a counterflow configuration: air stream enters in segment 1 and exits segment 4, while hydrogen flow enters in segment 4 and exits in segment 1.

To predict the Ce distribution during each protocol, experimentally obtained by XRF and already reported in Colombo et al. [9], an innovative model framework was developed and here presented for the first

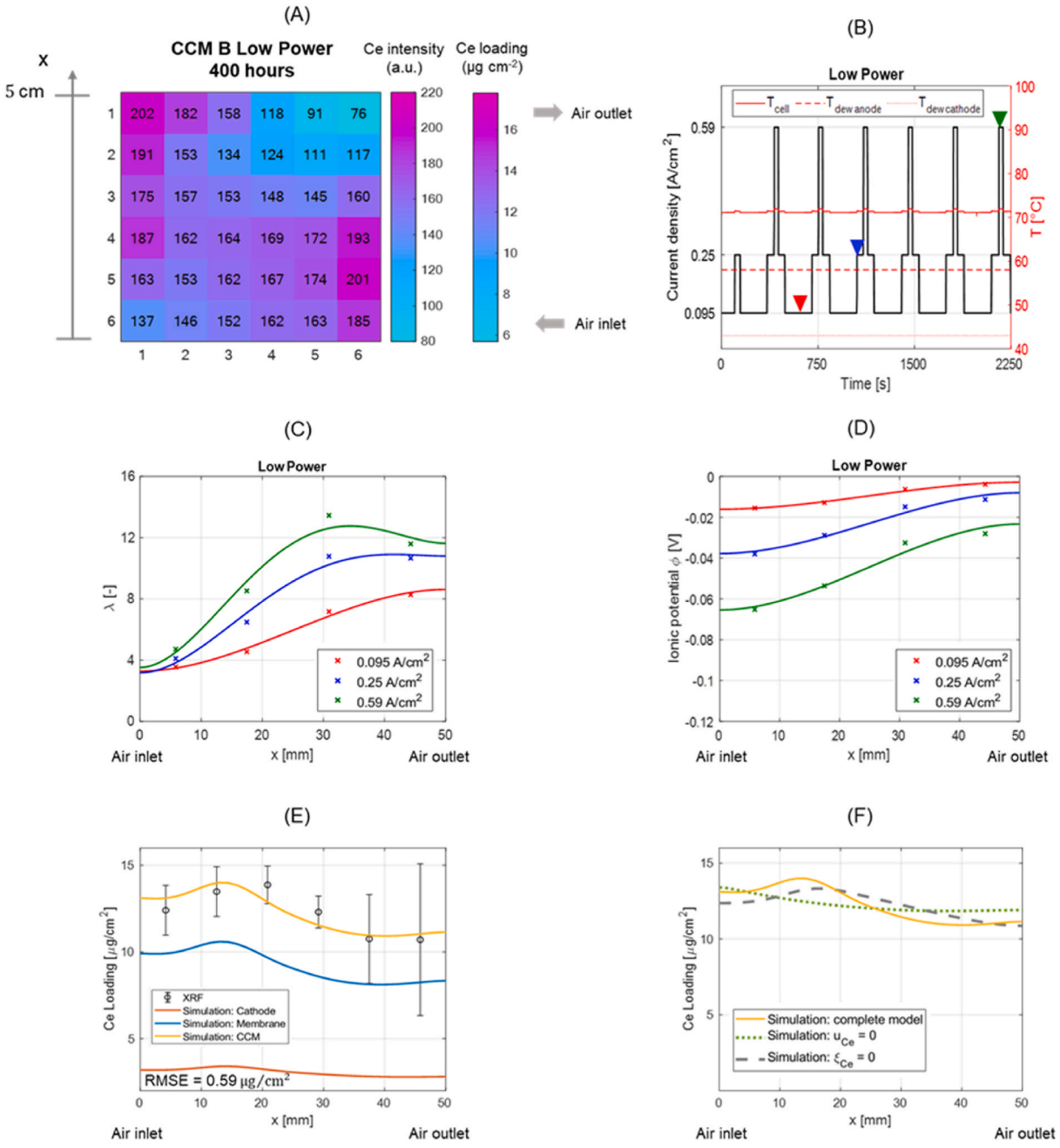

Fig. 5. (A) Heatmap of Ce loading obtained by XRF after 400 operating hours of the low-power protocol. Image reproduced from E. Colombo et al. [9] (https://doi.org/10.1016/j.jpowsour.2024.235962) under the CC BY license (http://creativecommons.org/licenses/by/4.0/). (B) Current density profile and cell temperature (red solid line) during the low-power protocol. The dew point at anode and cathode side are represented by the red dashed and dotted lines respectively. (C) In-plane water content and (D) ionic potential in the PEM domain for three different current densities of the low-power protocol. The markers represent the values provided by the 1+1D PEMFC model while the solid lines represent the polynomial space functions. The profiles in cathode CL are shown in Fig. S8. (E) In-plane Ce distribution after 400 operating hours of the low-power protocol. Comparison between XRF data and model simulations. In yellow the overall Ce loading in the CCM, while in blue in PEM, and in red in cathode CL domains. (F) Impact of ionic potential (grey line) and RH gradient (green line) on Ce ions transport under the operating conditions of the low-power protocol. Comparison with the complete model (yellow line). (For interpretation of the references to colour in this figure legend, the reader is referred to the Web version of this article.)

time (Fig. S6(A)). Such framework couples the 1D in-plane Ce transport model previously detailed (Equation (2)) with a 1+1D PEMFC performance model. In principle, Ce ions can be transported across both anode and cathode CLs and the membrane but, since during the operation Ce ions will mostly move through-plane towards the cathode CL due to the lowest ionic potential [51], only the in-plane transport inside the PEM and CCL domains will be considered in the following analysis neglecting, therefore, the planar transport in ACL. As shown in Fig. S6(A) and previously described in Section 3.1, the 1D in-plane Ce transport model requires some specific parameters as inputs:

- The initial cerium concentration in CCL and PEM domains, obtained by a through-plane analysis;
- The local water content λ and the local temperature T in the in-plane direction for each current step of the protocol, which are needed to compute the Ce diffusion coefficient, D_{Ce} and the migration

Table 4
Average cerium content over one cycle of each protocol expressed as Ce ion-exchanged fraction and loading in cathode CL and membrane. The values are obtained through the 1D through-MEA performance model. For the anode CL, it is assumed that the amount of cerium after one cycle is negligible due to migration towards cathode side.

DLC	Low Power		High Power		Complete Cycle	
Domain	CCL	Membrane	CCL	Membrane	CCL	Membrane
f_{Ce} [%]	6.9	5.7	9.0	4.1	8.5	5.4
Cerium loading [μg/cm^2]	2.2	8.6	2.8	6.2	2.7	8.1

coefficient, u_{Ce}. According to the assumption previously mentioned, these parameters are needed for both the CCL and PEM domains;

- The RH in the in-plane direction, in both CCL and PEM domains, which is needed to compute the term $\nabla \ln a_w$, which represents the driving force responsible for cerium ions transport due to water activity gradient;
- The ionic potential gradient, $\nabla \Phi_{ionic}$, in the in-plane direction for both the CCL and the PEM domains, which represents the driving force responsible for cerium ions migration.

The input parameters of the in-plane cerium transport model are provided by a 1+1D transient non-isothermal and multiphase PEMFC model through which the performance of the fuel cell at the beginning of life are simulated for each one of the protocols of interest. The complete description and validation of this model is reported in a previous paper [24], which reproduces the performance data for the same CCM and DLC protocol analysed in this manuscript. It should be noted that the 1+1D PEMFC performance model considers diffusion media and catalyst layers as isotropic and homogeneous. It solves kinetics, heat transfer and water transport in three phases: liquid, vapor, and dissolved in the ionomer, the latter including both diffusion and electro-osmotic drag fluxes. The reader can refer to Ref. [24] for all the related parameters and equations.

It is worth noting that the performance model consists in a 1+1D geometry, focusing on the through-the-membrane and the along-the-channel directions. The latter, as shown by Fig. S6(B), is discretized in eight control volumes. Therefore, the 1+1D model outputs are provided for eight discrete positions along the flow-field. However, since the objective of this work is to simulate in-plane cerium transport, the outputs were reduced to four x-direction coordinates -one for each cell segment- by averaging the relevant variables between each pair of adjacent control volumes (Fig. S6(B)). Furthermore, the 1+1D model is also discretized along the through-plane direction: specifically, the membrane is divided into ten control volumes of same dimensions while the cathode CL consists of only one layer [24]. For the cathode domain, the ionic potential is evaluated at the PEM/CCL interface, while for the membrane domain it is evaluated in its middle. Regarding the membrane water uptake, the mean value across all the ten layers is considered, which is then corrected to account for the effect of Ce ion-exchange fraction and RH as already mentioned in Section 3.1. Same considerations are valid for the water uptake of the cathode CL. Regarding the temperature, it was considered constant in the in-plane direction since its spatial variation resulted almost negligible (<4 °C).

First, it is necessary to assess the actual Ce concentration in the PEM and CCL domains by simulating the Ce ions transport in the through-the-membrane direction. For this purpose, a 1D through-MEA transient non-isothermal and multiphase PEMFC model is used, which represents a simplification of the 1+1D PEMFC model previously described. Starting from the initial Ce concentration of the pristine CCM (5.5%), it was possible to quantify the average Ce concentration in both CCL and PEM domains throughout a cycle of each dynamic load protocol under analysis. Such information was then provided as an input to the in-plane Ce transport model. The implementation of the governing equations accounting for Ce transport in the 1D through-MEA model is completely described in the Supplementary Material, and here not reported for brevity.

Model results confirm that the amount of Ce ions in the anode CL is negligible with respect to the concentration obtained in the PEM and CCL domains which, therefore, proves the validity of the before mentioned assumption of neglecting anode CL in the in-plane simulations. In Table 4, the initial amount of Ce in CCL and PEM domains are reported for each protocol.

The DLC protocols considered in this work are dynamic driving cycles, namely they are made by several current steps during which each variable of interest is characterized by its specific dynamic. Therefore, starting from performance simulations at beginning of life obtained through the 1+1D PEMFC model, for each current step and for each in-plane coordinate, the time integral mean value of water content, RH, T and ionic potential is computed and subsequently fitted with a polynomial space function, while considering a null derivative at the extremes of the domain. All these functions are then saved and given as an input to the in-plane Ce transport model which, depending on the protocol current setpoint, selects the proper function. Then, by applying the methodology just explained, the LP, HP and the complete DLC protocols are simulated. The main results are presented in the next section.

4.2. *In-plane cerium distribution: low-power protocol*

The low-power protocol previously described is now analysed in details. As already mentioned, it was repeated for 400 h, at the end of which the radical scavenger distribution was mapped [9]. The Ce redistribution predicted by the model framework described above is here compared to this experimentally measured profile, to identify the main stressors influencing cerium in-plane mobility.

Fig. 5(A) shows Ce redistribution after 400 operating hours: an heterogenous trend was observed, with cerium accumulation at the air inlet, while a depletion was observed towards the outlet. This trend is captured by the model, whose results are reported in Fig. 5(E) and compared to the data acquired in the elemental analysis performed by micro-XRF technique. For clarity, the XRF data shown in Fig. 5(E) were derived by calculating the arithmetic mean of each row in the map presented in Fig. 5(A). The error bars represent the deviation of the individual data points in each row from the mean values. The in-plane Ce loading profiles for both the cathode CL only (red line) and for the membrane only (blue line) are reported as estimated by the model. By summing the cerium loading in the CCL and the PEM it is possible to get the overall Ce loading (yellow line) which, as it can be seen, is consistent with the experimental data. The RMSE, indeed, is equal to 0.59 $\mu g_{Ce} cm^{-2}$. Specifically, the resulting overall cerium loading profile shows an accumulation towards the air inlet region and, more precisely, for an in-plane x coordinate equal to 10 mm, where the loading is around 13 $\mu g_{Ce} cm^{-2}$, which corresponds to a Ce ion-exchanged fraction equal to 9%. On the other hand, the minimum cerium loading is observed at the air outlet region. This observed Ce redistribution is consistent with the work of Lai et al. [21], where the authors observed a radical scavenger transport towards the driest regions of the cell after the application of an accelerated protocol which cycled the current between 0.05 and 1.2 Acm^{-2} at low inlet RH (30%).

To understand the reason of such heterogeneity in distribution, it is helpful to comment the water content and the ionic potential profiles in the membrane, which are shown in Fig. 5(C) and (D) for the three different current steps representative of the low power operating mode, graphically shown in Fig. 5(B) with three coloured triangles. By comparing the cerium distribution obtained with the water uptake and ionic potential profiles, it is possible to identify the drivers responsible for radical scavenger transport. As shown in Sections 3.2 and 3.3, Ce ions migrate towards regions characterized by lower ionic potentials and water activity, i.e. lower RH. Therefore, it is not surprising to detect that Ce ions are accumulated close to the air inlet region and depleted at the

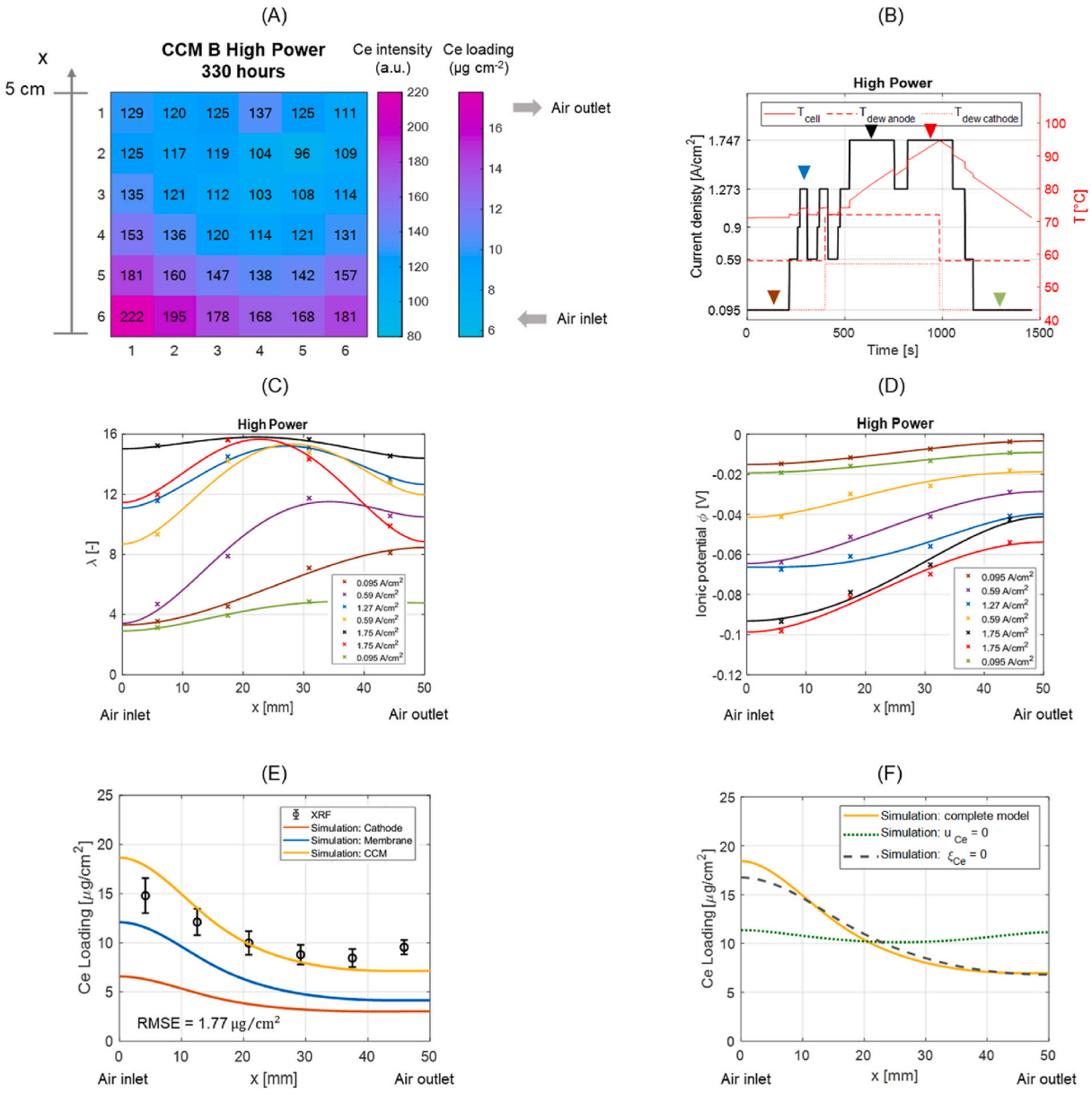

Fig. 6. (A) Heatmap of Ce loading obtained by XRF after 330 operating hours of the high-power protocol. Image reproduced from E. Colombo et al. [9] (https://doi.org/10.1016/j.jpowsour.2024.235962) under the CC BY license (http://creativecommons.org/licenses/by/4.0/). (B) Current density profile and cell temperature (red solid line) during the protocol. The dew point at anode and cathode side are represented by the red dashed and dotted lines respectively. (C) In-plane water content and (D) ionic potential in the PEM domain for seven different current densities of the high-power protocol. The markers represent the values provided by the 1+1D PEMFC model while the solid lines represent the polynomial space functions. The profiles in cathode CL are shown in the Supplementary Material. (E) In-plane Ce distribution. Comparison between XRF data and model simulations. In yellow the overall Ce loading in the CCM after 330 h, while in blue and red the Ce loading in PEM and cathode CL domains. (F) Impact of ionic potential (grey line) and RH gradient (green line) on Ce ions transport under the operating conditions of the high-power protocol. Comparison with the complete model (yellow line). *(For interpretation of the references to colour in this figure legend, the reader is referred to the Web version of this article.)*

air outlet. Indeed, as shown in Fig. 5(C), the low relative humidity of the gas at cathode channel inlet (i.e. 30%) strongly penalizes the water uptake of the air inlet region. Then, thanks to the progressive water production and accumulation, the water content increases along the flow-field channel. At the same time, the ionic potential profile is not homogeneous in the in-plane direction too: indeed, depending on local fuel cell performance, it increases from air inlet to air outlet due to a progressive decrease of the ionic loss associated with a better ionomer hydration state. Anyway, the Ce loading peak is shifted from the x coordinate equal to 0 to around 10 mm: this effect is attributed to the significantly limited mobility of Ce ions in a portion of MEA characterized by very low water contents. Being the diffusive, migrative and water activity gradient terms of the cerium flux all functions of the diffusion coefficient, a reduction of D_{Ce} due to a lower water content slows down Ce ions transport.

In the cathode domain, the cerium loading profile shows the same trend already discussed for the membrane. Ionic potential and water content are reported in the Supplementary Material (Fig. S8(B)–(C)) and, being very similar to the one already described for the membrane, they are here not furtherly discussed. However, it is worth noting that the Ce profile in the CCL results to be much flatter with respect to the one of the PEM. This behaviour may be explained by the lower ionomer fraction in the cathode which, therefore, according to Equation (2), strongly reduces cation mobility.

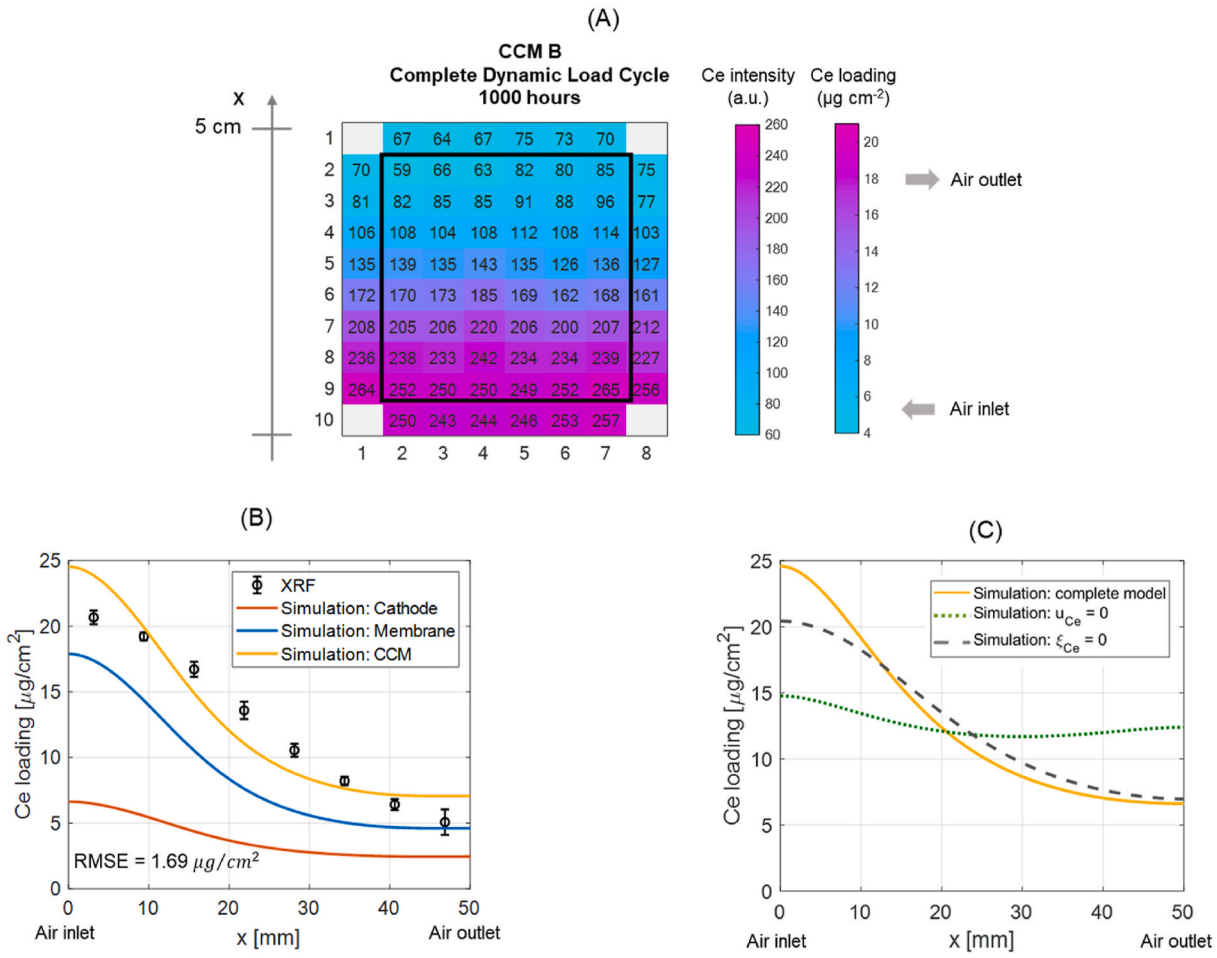

Fig. 7. (A) Heatmap of Ce loading obtained by XRF after 1000 operating hours of the complete DLC protocol. Image reproduced from E. Colombo et al. [9] (https://doi.org/10.1016/j.jpowsour.2024.235962) under the CC BY license (http://creativecommons.org/licenses/by/4.0/). (B) In-plane Ce distribution. Comparison between XRF data and model simulations. In yellow the overall Ce loading in the CCM after 1000 h, while in blue and red the Ce loading in PEM and cathode CL domains. (C) Impact of ionic potential (grey line) and RH gradient (green line) on Ce ions transport under the operating conditions of the high-power protocol. Comparison with the complete model (yellow line). *(For interpretation of the references to colour in this figure legend, the reader is referred to the Web version of this article.)*

In the light of this analysis, the water content and the ionic potential gradients, which push cerium ions in the same direction, seem to be the two main drivers responsible for the cerium redistribution observed after 400 h of the LP DLC protocol. To quantify the role played by the RH and ionic potential gradient on the final in-plane cerium redistribution obtained after 400 h, the protocol was simulated neglecting either the migrative or the water activity gradient contribution. The results are shown in Fig. 5(F): as already discussed, this operating mode is characterized by a strong in-plane heterogeneity in terms of water activity. Nevertheless, considering only the RH gradient contribution ($u_{Ce} = 0$), the cerium loading profile would have a different trend, flatter in the middle and with a more promoted accumulation towards air inlet. Therefore, the results shown in Fig. 5(F) suggest that the shape of the Ce loading profile at the end of the protocol is mainly related to the ionic potential gradient contribution.

4.3. In-plane cerium distribution: high-power protocol

Cerium distribution after 330 h of the high-power DLC protocol is shown in Fig. 6(A). As already discussed for the LP protocol, a cerium accumulation towards air inlet is observed. However, compared to the Low Power results, where the minimum of the Ce loading was located at the air outlet, for this protocol it is located around an in-plane coordinate equal to 30 mm, which corresponds to the third segment of the cell.

To explain these results, it is necessary to look at the in-plane water content and ionic potential profiles during the HP protocol, which are shown in Fig. 6(C) and (D) for the membrane domain. Please, refer to Fig. S8(E)–(F)) for the profiles in cathode CL.

The position of the maximum loading coincides with the minimum of the ionic potential, which is located exactly at air inlet region, as for the LP protocol. Moreover, also the minimum water content is at the cathode inlet, which further contributes to drive cerium ions towards such region of the cell. On the contrary, as it is visible in Fig. 6(D), the ionic potential profile has its maximum at the air outlet region which, therefore, should be the region characterized by the largest cerium depletion. However, as shown in Fig. 6(C), for the highest current densities of the cycle (blue, red and black lines) the water content has its maximum around an in-plane coordinate equal to 30 mm and then it decreases going towards the air outlet region due to a net water flux from cathode to the anode side, as highlighted in Ref. [24]. This can explain the reason why the minimum of the cerium loading profile is shifted towards an in-plane coordinate equal to 30 mm. This result confirms, once again, the key interplay between water content and ionic potential gradient on cerium ions transport. Moreover, it is interesting to highlight the more important Ce heterogeneity observed during this operating mode: after 330 operating hours, indeed, the loading varies between 9 and 15 $\mu g_{Ce} cm^{-2}$, which is a wider range with respect to the single LP protocol (10–13 $\mu g_{Ce} cm^{-2}$). The main difference in radical

scavenger redistribution is attributable to the operating conditions, which strongly differ from the LP to the HP operating modes. In particular, the low power working mode is characterized by a current density ranging between 0.095 Acm^{-2} and 0.59 Acm^{-2} and by a constant operating temperature around 71 °C. The high-power mode, instead, is characterized by current densities ranging from 0.095 Acm^{-2} to 1.75 Acm^{-2}. Furthermore, the operating temperature is not constant as in the LP, but increases up to 90 °C. As discussed in Section 3.1, Ce ions diffusion coefficient strongly depends on the operating conditions and, in particular, it increases with both temperature and water content. Therefore, consistently to Figs. 5(C) and 6(C)), the diffusion coefficient of Ce ions will be higher under the high power protocol. Moreover, the higher loads required to the fuel cell in the HP operation also increase the ionic potential gradients, which furtherly contribute to accelerate radical scavenger redistribution.

Again, the trends of the cerium loading profiles of membrane and cathode are quite similar. In terms of absolute values, the difference with the Ce loading in the membrane domain is less marked with respect to the low power protocol and this may be attributed to the higher current densities achieved during this operating mode, which drive much more cerium ions towards cathode CL, as highlighted also by the higher Ce ion-exchange values reported in Table 4. Moreover, it is worth noting that the Ce loading profile in the cathode, once again, is flatter with respect to the one in the membrane since, although a higher water uptake (see Fig. S8(E)) and therefore a higher cerium diffusion and migration coefficients, the lower ionomer fraction in cathode CL reduces cation mobility with respect to the PEM domain. The tomography analysis carried out on the aged sample tested for 330 h of the HP protocol, and reported in Fig. S12, supports model outcomes suggesting that the much more complex structure of the cathode CL, and in particular the presence of several cracks, may furtherly slows down the in-plane radical scavenger transport which, therefore, finds in the PEM domain a preferential pathway for diffusion. Comparing the air inlet and outlet regions at the end of the HP protocol, similar membrane thicknesses are observed via a tomography analysis: 11.4 ± 3 μm and 11.0 ± 3 μm, respectively, with the slightly lower value in the outlet region being masked by the statistical deviation.

Lastly, in Fig. 6(F) the effect of either the ionic potential or of the RH gradient on the high-power protocol is shown. Since this operating mode is characterized by a less important planar water activity gradient between air inlet and outlet with respect to the LP protocol, and because of a much more relevant in-plane ionic potential gradient, the main driving force responsible for cerium mobility is actually represented by the ionic potential gradient under the HP operation. Indeed, considering the only RH gradient contribution, the cerium loading profile would be characterized by two different regions of accumulation, one at the air inlet and one at the air outlet, and a region of depletion corresponding to the middle part of the cell. This result, which is coherent with the water content profile shown in Fig. 6(C), however, is not consistent with the elemental analysis carried out by the micro-XRF. These results, therefore, further confirm the key role played by the ionic potential gradient under the high-power operating conditions.

4.4. *In-plane cerium distribution: complete dynamic load cycle protocol*

The complete DLC protocol is a combination of the LP and HP operating modes previously described. This is reflected also by the cerium redistribution quantified after 1000 operating hours: the high-power mode, and in particular its high ionic potential gradient, strongly drives the cerium transport towards the air inlet region where, indeed, as highlighted from Fig. 7(A) and (B) and already described in previous section, is located the maximum of the Ce content. Furthermore, since the LP part represents the 66% of the overall DLC protocol, the high RH gradient established during this operating mode contributes to further drive cerium ions towards the air inlet and to reduce the cerium content at the air outlet. It is interesting to underline that, with respect to the single operating modes, the radical scavenger transport is even more exacerbated in the case of the complete DLC protocol, as highlighted by the highest heterogeneities in terms of Ce loading. Indeed, starting from a homogeneous f_{Ce} of approximately 5.5% at BoT, the Ce ion-exchange fraction ranges between 2% and 13.5% after 1000 h, a result that can be explained by the longer duration of the protocol under analysis.

As it can be detected from Fig. 7(B) and also confirmed by a RMSE equal to 1.69 $\mu g_{Ce} cm^{-2}$, small differences arise between model simulations and experimental data. Ce accumulation at air inlet is correctly predicted by the model even though the absolute value is slightly overestimated. This result may be associated with an overestimation of the mobility coefficients and, in particular, of the diffusion coefficient D_{Ce}. Indeed, as already explained in Section 3.1, D_{Ce} was calibrated on experimental data taken from the literature [12,14,27] and representative of cerium ions diffusion under different operating conditions, i.e. water content and temperature. However, the complete DLC protocols analysed in this work, especially in its HP region, is characterized by a short operating period during which the cell temperature increases beyond 90 °C (see Fig. 6(B)) which, however, is out of the range in which we calibrated the diffusion coefficient. Therefore, even if the results shown for the hydrogen pumping test at 90 °C and for the single HP protocol, which lasted 4 h and 330 h respectively, seem to suggest the validity of the D_{Ce} expression used in this work, in a protocol characterized by a longer duration (1000 h) it may lead to slightly overestimate cerium ions mobility. For this reason, in the next section a sensitivity analysis on the diffusion coefficient is carried out. Another point to consider and that may explain the small differences observed between model simulation and the experimental Ce redistribution is the fact that, during real operation, different degradation mechanisms take place, responsible for the progressive cell voltage loss. A heterogeneous degradation of the cathode catalyst layer was observed during ageing [19,52], both in terms of electrocatalyst active surface area loss and increased pressure independent oxygen transport resistance. Changes in local current densities occurred, particularly evident in the air inlet region, which can affect the local ionic potential. This effect can be, at least partially, attributed to the same redistribution of radical scavengers over the CCM active area. As a result, ageing may progressively reduce the in-plane ionic potential gradient, slowing down the Ce transport, and partly explain the discrepancy between modelling and experimental observations, as the current model assumes constant driving forces throughout the test duration. Future studies could include the development of a degradation framework and the interplay between cerium cations migration and PEMFC performance.

The effects of the single driving forces of RH and ionic potential gradients on the complete driving cycle load protocol are shown in Fig. 7 (C). Considering the RH contribution only, more relevant for the LP part of the test (which represents the 66% of the overall protocol) the high water content gradient contributes to drive cerium ions towards the air inlet. Nevertheless, both the intensity of the cerium peak and the shape of the loading profile would not be correctly captured without considering the ionic potential gradient contribution, especially as regards the depletion at the air outlet region. This analysis, therefore, highlights the key role played by the planar ionic potential gradient on radical scavenger migration under automotive-representative operating conditions.

As we discussed in the introduction section, the radical scavenger redistribution observed in all the three driving cycle protocols has an impact on both PEMFC performance and durability. Ce accumulation could decrease PEMFC performance, especially at high current density, highlighting its negative impact on local oxygen mass transport resistance: for instance, at 1.8 Acm^{-2} and under the operating conditions of the driving cycle protocol, the voltage loss after 1000 h of the complete DLC protocol is equal to 108 mV at the air inlet, that is 1.5 times more than the average cell behaviour [19]. Ce depletion, instead, accelerates membrane degradation increasing the hydrogen crossover current: for instance, at the air outlet, where a reduction in Ce content was observed,

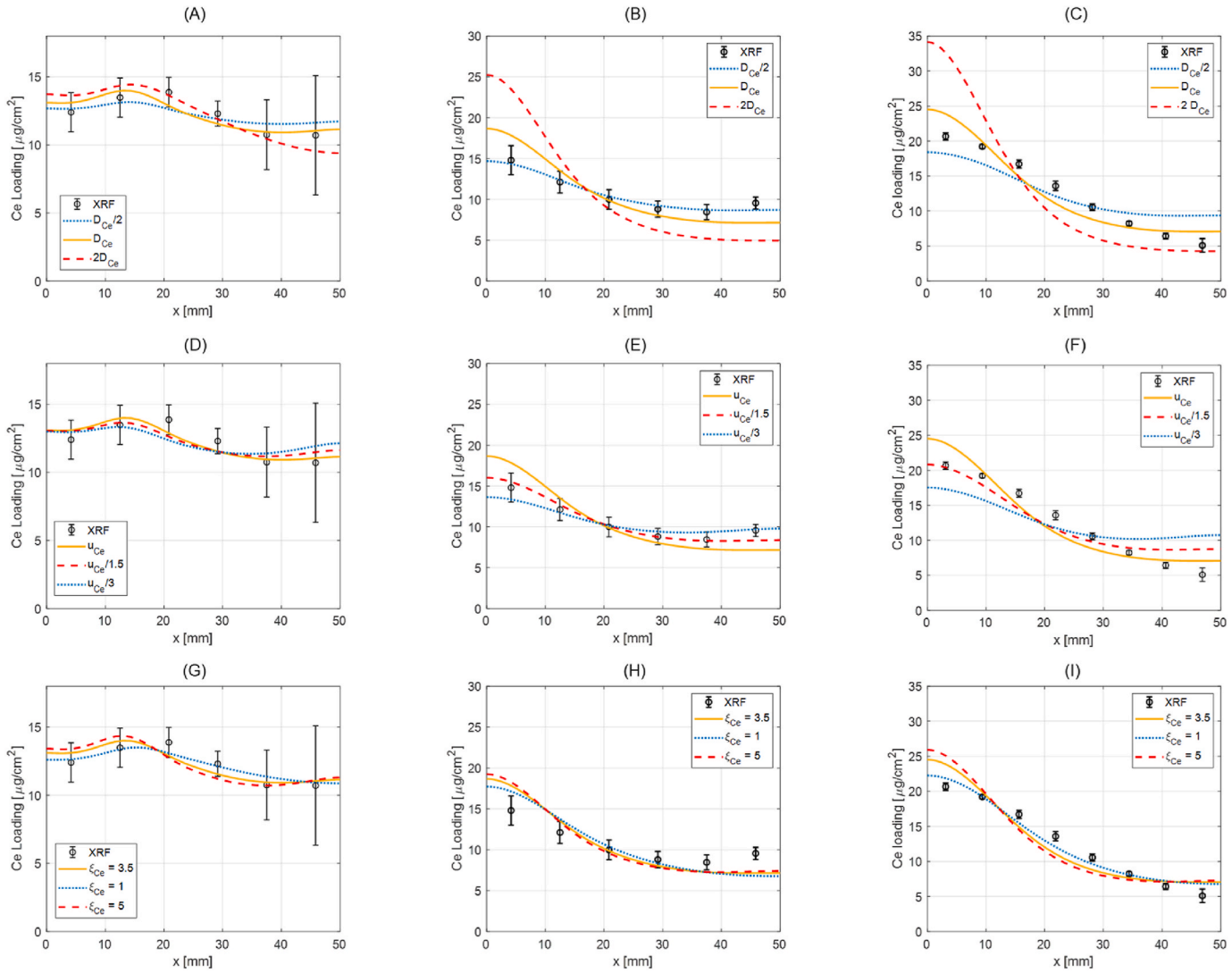

Fig. 8. In-plane Ce distribution. Comparison between XRF data and model simulations after (A) 400 h of the LP protocol, (B) 330 h of the HP protocol and (C) 1000 h of the complete DLC protocol, for different values of the diffusion coefficient D_{Ce}. Effect of coefficient u_{Ce} on in-plane Ce distribution. Comparison between XRF data and model simulations after (D) 400 h of the LP protocol, (E) 330 h of the HP protocol and (F) 1000 h of the complete DLC protocol. Effect of coefficient ξ_{Ce} on in-plane Ce distribution. Comparison between XRF data and model simulations after (G) 400 h of the LP protocol, (H) 330 h of the HP protocol and (I) 1000 h of the complete DLC protocol.

the crossover current after 1000 h of the complete driving cycle protocol increases 20% more than in the other regions of the cell [9]. To quantify the impact of Ce content on the membrane chemical degradation rate, Johnson et al. [53] developed a mathematical model to correlate the fluoride emission rate (FER), representative of the chemical stability of PFSA membranes, to the operating conditions and the radical scavenger content; in particular, the chemical degradation rate decreases with the Ce content. By applying their proposed formulation, it is estimated a reduction in the FER at the air inlet region equal to 49% for the complete protocol. On the contrary, because of Ce depletion, at the air outlet the FER increases by 53%, highlighting the higher chemical degradation rate induced by a lower scavenging efficacy. Additional details have been added in Table S2.

The results discussed so far refer to 1000 h of automotive operation on a lab scale single-cell. Clearly, the impact of this phenomenon and its time scale is also affected by MEA dimensions: indeed, moving from a 5 cm long cell (representative of a lab-scale single cell) to a 40 cm long cell (more representative of real operation), Ce redistribution requires more time to take place. Indeed, as it is shown by Fig. S13(A), after 8000 h of the complete DLC protocol, that is the durability target by the end of 2050 for light-duty vehicles [1], the maximum of the Ce loading decreases by a factor 3.6 when the MEA length increases from 5 cm to 40 cm. In the same way, also the minimum Ce content varies with the in-plane transport coordinate, and it increases by a factor 10 increasing the MEA length from 5 cm to 40 cm. The lab-scale test hence accelerates the process, that is anyway consistently evolving with respect to the application. Indeed, Fig. S13(B) confirms that, independently on the size of the cell, Ce accumulates at the air inlet and depletes at air outlet. Therefore, mitigation strategies must be developed especially considering that the high operating temperatures, higher loads and the target of 30000 h of operation for the heavy-duty application can further promote Ce ions transport. In this scenario, advances in the development of more stable radical scavengers have been done recently. For instance, a current strategy consists in the adoption of cerium oxides (ceria nanoparticles) instead of Ce ions as radical scavengers, which offer the advantage to be much more stable. However, under the typical PEMFC operating conditions, ceria-based free radical scavengers have the tendency to agglomerate and dissolve in Ce^{3+}/Ce^{4+} which are characterized by a significant mobility [54]. To address this issue, various support materials have been investigated. In particular, acid-resistant ceramic or

oxide materials have been employed to improve the overall stability of ceria nanoparticles as well as their scavenging kinetics [54]. Agarwal et al. [55] studied cation size selective agents to reduce Ce mobility within PFSA membranes. They synthesized an organometallic Ce complex which, not migrating in presence of a potential gradient, allows to increase by 80% the chemical durability. In recent studies [56], the possibility to adopt Cerium-based Mixed Metal Oxide as radical scavenger was also explored. For example, Oh et al. [56] developed a perovskite-structured multi-metal oxide which, having high radical scavenging properties and good structural stability, allowed to enhance membrane durability with respect to membranes adopting only CeO_2 as scavenger.

4.5. Effect of diffusion, migration and electro-osmotic drag coefficients on cerium ions transport under automotive-representative operating conditions

The modelling analysis carried out in previous sections pointed out that the interplay among Ce concentration, water content and ionic potential gradients is responsible for cerium ions transport under automotive-representative operating conditions. The modelling of each one of these mechanisms, as it is reported in Equation (2), requires the definition of specific coefficients, namely D_{Ce}, ξ_{Ce}, and u_{Ce}. The first, as described in Section 3.1, was calibrated from data available in the literature [12,14,27] and it proves to correctly describe cerium ions diffusion for Nafion XL and NR 211 membranes. Nevertheless, it is not yet clear as membrane properties, such as the EW or the presence/absence of the mechanical reinforcement, may influence cation mobility. Indeed, as recently highlighted in the work of Shinozaki et al. [16], for a thin reinforced PFSA membrane the through-plane diffusion coefficient is approximately half that of a thick non-reinforced membrane. Therefore, it is reasonable to assume that D_{Ce}, and in particular the dependence of the diffusion coefficient from water content and temperature, may slightly vary from one membrane to another. In this work, for instance, the used commercial CCM adopts a 18 μm thick membrane with mechanical reinforcement. For this reason, a sensitivity analysis was conducted to understand how the cerium transport may be influenced by a change of this parameter, in particular by dividing and multiplying the D_{Ce} coefficient by a factor of 2.

The main results of this sensitivity analysis are shown in Fig. 8(A)–(B)–(C): it is evident that, for the LP operating mode, being characterized by lower temperatures and water contents, the in-plane cerium distribution predicted by the model does not change significantly by multiplying or dividing the diffusion coefficient by a factor of 2. For the high power and complete DLC protocols, instead, the results change with the diffusion coefficient and, in particular, as shown in Fig. 8(B) and (C), by halving D_{Ce} it would be possible to improve the model accuracy for the HP even though, for the complete protocol (Fig. 8(C)), Ce accumulation at the air inlet would be underestimated as well as the depletion at the air outlet region suggesting that, as it will be discussed in a while, the radical scavenger redistribution profile is more affected by a change in the migration coefficient rather than the diffusion coefficient.

An additional sensitivity analysis was carried out on the migration coefficient u_{Ce} since, as reported in the literature [14,16], the validity of the Einstein relation is still under discussion. As already discussed in Section 3.2, in the work of Baker et al. [14], the mobility coefficient u_{Ce} -fitted by the authors' model- is 1.5 times lower than the one that would be obtained by the Einstein relation. In the work of Shinozaki et al. [16], instead, u_{Ce} is approximately divided by a factor of 3 to account for the deviation caused by the mixing energy between protons and metal cations. As a consequence, a sensitivity analysis was carried out for all the three protocols by comparing the reference case, in which the Einstein relation is adopted, with two additional cases where the migration coefficient is divided by a factor of 1.5 and 3 respectively. Once again, as it is shown in Fig. 8(D)–(E)–(F), the LP protocol does not seem to be significantly affected by a variation of u_{Ce}. Much more differences can be detected for the HP and complete protocols, where the local operating conditions leads to an increase of the diffusion coefficient and, therefore, of u_{Ce}. As highlighted by Fig. 8(E)–(F), a reduction of the migration coefficient could help to improve the adherence with experimental data. In particular, the case $u_{Ce}/1.5$ seems to be the best one. Since, according to our analysis, the ionic potential gradient contribution seems to be most influential one on radical scavenger transport, a further sensitivity analysis was conducted to understand how the uncertainty of this parameter affects the long-term predictions. For this purpose, the complete driving cycle protocol was simulated for 8000 h in the case of a 20 cm × 30 cm cell, being it more representative of real applications. This analysis, reported in Fig. S13(B), revealed that dividing the migration coefficient computed by the Einstein relation by a factor of 1.5 and 3 does not significantly affect the prediction capabilities of the model. After 8000 h, Ce accumulation at the air inlet ranges between 13.7 and 14.9 $\mu g_{Ce} cm^{-2}$ while Ce depletion at the air outlet varies between 10.9 and 11.9 $\mu g_{Ce} cm^{-2}$ depending on the values assumed of u_{Ce}.

Lastly, due to the uncertainty on the electro-osmotic drag coefficient for trivalent ions, a sensitivity analysis was carried out by setting the coefficient ξ_{Ce} equal to 1 and 5 in addition to the reference value of 3.5 since, consistently to the analysis already shown in Fig. S5. As highlighted by Fig. 8(G)–(H)–(I), a reduction or an increase in the electro-osmotic drag coefficient, at fixed water content gradient between air inlet and air outlet, does not change significantly the final Ce loading profile whose shape is unchanged. On the contrary, the Ce loading peak located at the air inlet is influenced by a variation of the coefficient ξ_{Ce}: in particular, by doubling ξ_{Ce} an increase in the Ce peak is observed -less adherent to the experimental data-, but the variation is anyway limited.

5. Conclusion

Based on the Nernst-Planck equation, a 1D in-plane Cerium transport model was calibrated and validated.

Experimental data taken from the literature were used to calibrate the diffusion coefficient for Ce ions and the effect of Ce ion-exchange fraction on the protonic conductivity and water uptake of the membrane. Concerning the migration coefficient, the Einstein relation was adopted. The in-plane Ce transport model was validated on both tailored and literature data gathered via hydrogen pumping experiments and representative of different membranes, different initial cerium concentrations and various operating conditions (T, RH). The model succeeded in the predictions and revealed the critical role played by the relative humidity and the temperature: indeed, at fixed applied potential, a decrease in the RH strongly reduces cation mobility. On the other hand, an increase in the operating temperature accelerates Ce ions transport. At fixed operating conditions, also the initial Ce ion-exchange fraction has an impact on cation mobility: indeed, a reduction in f_{Ce} gives rise to a flatter migration profile, which can be mainly attributed to a lower contribution of the migrative flux.

To study the effect of water content gradient on cerium transport, ad-hoc tests were carried out: Ce-doped membranes were placed into a vessel containing 700 ml of deionized water at 80 °C such that the lower part of the membrane was submerged while the remaining part was above the liquid-air interface, where the temperature was set at 80 °C with a 5% RH. The XRF analysis revealed a transport of cerium ions from the high RH side to the low RH side and a modelling analysis allowed to fit an electro-osmotic coefficient, ξ_{Ce}, equal to 3.5.

The 1D in-plane Ce transport model was then coupled with an existing 1+1D PEMFC performance model to develop an innovative model framework able to identify the main drivers responsible for Ce migration under operating conditions that are representative of the automotive operation. In particular, the complete DLC protocol defined in the frame of the European ID-FAST project and both single low-power and high-power operating modes were analysed. Model simulations, coherently with the XRF analysis outcomes, revealed a significant in-

Table 5
Summary of the drivers responsible for radical scavenger redistribution, related transport parameters and influence, with some critical considerations.

Driving Force	Transport parameter	Influence	Critical considerations
Concentration gradient	Ce diffusivity: $D_{Ce} = D_{Ce}(\lambda, T)$	• In-plane, it counteracts ionic-potential and water activity gradients	• Necessity to investigate the role played by membrane properties (e.g. thickness, reinforcement) on D_{Ce} • D_{Ce} directly impacts on migration process, being directly proportional to the migration coefficient
Ionic potential gradient	Ce migration coefficient: $u_{Ce} = \frac{z_{Ce}FD_{Ce}}{RT}$	• It affects the intensity of in-plane transport • It determines the regions of accumulation/depletion • Quantified as the main driver, especially during high power operation	• Einstein relation still valid, but more accurate descriptions could be researched
Water activity gradient	Ce electro-osmotic drag coefficient: ξ_{Ce}	• It affects the intensity of in-plane transport • Lower contribution rather than ionic potential gradient under in-plane automotive-representative operating conditions	• Future works to address the physical mechanism behind Ce transport due to RH gradient

plane Ce redistribution during the application of all the three different protocols, with an accumulation at air inlet, characterized by the lowest ionic potential and water content, and a depletion at the air outlet, characterized by the highest ionic potential and water content. The effect is more pronounced during high-power operation, highlighting the critical role of high current densities in driving radical scavenger redistribution, an aspect even more relevant for heavy-duty applications. Furthermore, the model framework developed in this work allowed to identify the key role played by the planar ionic potential gradient on cerium transport: indeed, for the high-power and for the complete DLC protocols, the water content gradient alone may not be sufficient to explain the experimentally observed radical scavenger redistribution whose intensity and shape, as highlighted by Table 5, seems to be mainly controlled by the ionic-potential gradient.

Lastly, a sensitivity analysis was carried out to investigate the influence of diffusion, migration and electro-osmotic drag coefficients on cerium transport, which are the parameters characterized by the highest uncertainty. Lowering the diffusion coefficient, cerium transport is slowed down; this effect is particularly evident for the HP protocol, and hence for the complete DLC, since it is characterized by the highest water content and temperature, hence most influenced by a variation of the diffusion coefficient: by halving D_{Ce} it would be possible to improve the adherence between model simulations and experiment. The HP and complete protocols are also sensitive to a variation of u_{Ce}: by dividing the migration coefficient by a factor 1.5, the experimental data would be even better reproduced by the model. A variation of the electro-osmotic drag coefficient, instead, does not change significantly cerium redistribution. Some variations, mainly concerning the maximum cerium peak achieved at air inlet, are observed for the HP and complete DLC.

Succeeding in the prediction, the proposed model framework represents a valuable diagnostic tool: indeed, if coupled with a semi-empirical or physical-based membrane degradation model, it may provide useful information about the impact of Ce ions transport on both PEMFC performance and durability. Consequently, it might also be used to develop possible mitigation strategies, both material-based or system control-based. At the same time, it might also be adopted to support the design of water management strategies aimed at avoiding excessive water activity gradient between air inlet and air outlet regions, especially under high loads operating conditions, more severe for what concern radical scavenger transport.

CRediT authorship contribution statement

Francesco Verducci: Writing – original draft, Visualization, Validation, Software, Methodology, Investigation, Formal analysis, Data curation, Conceptualization. **Livio Cultrera:** Writing – original draft, Validation, Software, Methodology, Investigation, Formal analysis, Data curation, Conceptualization. **Elena Colombo:** Writing – review & editing, Validation, Software, Methodology, Investigation, Formal analysis, Data curation, Conceptualization. **Aixeen Manuel Fontanilla:** Writing – original draft, Visualization, Software, Investigation, Formal analysis, Data curation. **Francesco Casamichiela:** Supervision, Software, Formal analysis, Data curation. **Davide Mazzucconi:** Visualization, Investigation. **Andrea Pola:** Funding acquisition. **Andrea Casalegno:** Supervision, Project administration, Funding acquisition. **Andrea Baricci:** Writing – review & editing, Supervision, Methodology, Conceptualization.

Declaration of competing interest

The authors declare that they have no known competing financial interests or personal relationships that could have appeared to influence the work reported in this paper.

Acknowledgments

The authors want also to thank Dr. Marco Cerchetti, who contributes to the realization of this work by the deposition of the Pt/C layer via Ultrasonic Spray Coating, and to Dr. Amedeo Grimaldi for his continuous support in the development of the model.

This work received funding from the Italian government (Ministero dell'Ambiente e della Sicurezza Energetica), under the program Progetto Permanent - Bando MITE PNRR Missione 2 Investimento 3.5 A - RSH2A_0O0012.

The authors gratefully acknowledge the support of the ISIS@MACH ITALIA Research Infrastructure, the hub of ISIS Neutron and Muon Source (UK), [MUR official registry U. 0008642.28-05-2020 April 16, 2020]. IM@IT is listed in the Italian Ministry of University and Research's Piano Nazionale delle Infrastrutture di Ricerca (PNIR 2021–2027) "in the broader notion of ISIS", and ISIS Facility and IM@IT are jointly listed in high priority RI's (see Table 6 page 30, note 38, PNIR in 2021–2027).

Part of this work has received funding from the MOST e Sustainable Mobility Center funded by the European Union Next-GenerationEU (PIANO NAZIONALE DI RIPRESA E RESILIENZA (PNRR) e MISSIONE 4 COMPONENTE 2, INVESTIMENTO 1.4 e D.D. 1033 June 17, 2022, CN00000023).

Appendix A. Supplementary data

Supplementary data to this article can be found online at https://doi.org/10.1016/j.jpowsour.2025.238538.

Data availability

Data will be made available on request.

References

[1] D.A. Cullen, K.C. Neyerlin, R.K. Ahluwalia, R. Mukundan, K.L. More, R.L. Borup, A. Z. Weber, D.J. Myers, A. Kusoglu, New roads and challenges for fuel cells in heavy-duty transportation, Nat. Energy 6 (2021) 462–474, https://doi.org/10.1038/s41560-021-00775-z.

[2] A.M. Baker, A.R. Crothers, K. Chintam, X. Luo, A.Z. Weber, R.L. Borup, A. Kusoglu, Morphology and transport of multivalent cation-exchanged ionomer membranes using perfluorosulfonic acid-cez+as a model system, ACS Appl. Polym. Mater. 2 (2020) 3642–3656, https://doi.org/10.1021/acsapm.0c00633.

[3] M. Chandesris, R. Vincent, L. Guetaz, J.S. Roch, D. Thoby, M. Quinaud, Membrane degradation in PEM fuel cells: from experimental results to semi-empirical degradation laws, Int. J. Hydrogen Energy 42 (2017) 8139–8149, https://doi.org/10.1016/j.ijhydene.2017.02.116.

[4] K.H. Wong, E. Kjeang, Mitigation of chemical membrane degradation in fuel cells: understanding the effect of cell voltage and iron ion redox cycle, ChemSusChem 8 (2015) 1072–1082, https://doi.org/10.1002/cssc.201402957.

[5] A.M. Baker, R. Mukundan, D. Spernjak, E.J. Judge, S.G. Advani, A.K. Prasad, R. L. Borup, Cerium migration during PEM fuel cell accelerated stress testing, J. Electrochem. Soc. 163 (2016) F1023–F1031, https://doi.org/10.1149/2.0181609jes.

[6] N. Macauley, A.S. Alavijeh, M. Watson, J. Kolodziej, M. Lauritzen, S. Knights, G. Wang, E. Kjeang, Accelerated membrane durability testing of heavy duty fuel cells, J. Electrochem. Soc. 162 (2015) F98–F107, https://doi.org/10.1149/2.0671501jes.

[7] N. Macauley, M. Lauritzen, S. Knights, E. Kjeang, Predicting membrane lifetime with cerium oxide in heavy duty fuel cell systems, J. Electrochem. Soc. 165 (2018) F780–F785, https://doi.org/10.1149/2.0271810jes.

[8] V.M. Ehlinger, A.R. Crothers, A. Kusoglu, A.Z. Weber, Modeling proton-exchange-membrane fuel cell performance/degradation tradeoffs with chemical scavengers, JPhys Energy 2 (2020), https://doi.org/10.1088/2515-7655/abb194.

[9] E. Colombo, A. Grimaldi, A. Baricci, M. Pak, Y. Morimoto, I.V. Zenyuk, A. Casalegno, In-plane redistribution of radical scavenger during PEMFC real-world automotive operation and impact on catalyst-layer local oxygen transport resistance, J. Power Sources 629 (2025) 235962, https://doi.org/10.1016/j.jpowsour.2024.235962.

[10] J. Chen, A. Goshtasbi, A.P. Soleymani, M. Ricketts, J. Waldecker, C. Xu, J. Yang, T. Ersal, J. Jankovic, Effects of cycle duration and test hardware in relative humidity cycling of a polymer electrolyte membrane, J. Power Sources 476 (2020) 228576, https://doi.org/10.1016/j.jpowsour.2020.228576.

[11] J. Liu, Y. Yin, J. Zhang, T. Zhang, X. Zhang, H. Chen, Mechanical degradation of catalyst layer under accelerated relative humidity cycling in a polymer electrolyte membrane fuel cell, J. Power Sources 512 (2021) 230487, https://doi.org/10.1016/j.jpowsour.2021.230487.

[12] F.D. Coms, A.B. LaLonde, Determination of Ce3+, Co2+, Mn2+ and Fe2+ diffusion coefficients in nafion® membrane, J. Power Sources 580 (2023), https://doi.org/10.1016/j.jpowsour.2023.233359.

[13] A.M. Baker, Y. Cai, J.M. Ziegelbauer, D. Agyeman-Budu, A. Woll, A. Kongkanand, R. Mukundan, R.L. Borup, Development of operando confocal microprobe X-ray fluorescence techniques to measure cation transport in PEM fuel cells, ECS Trans. 92 (2019) 107–117, https://doi.org/10.1149/09208.0107ecst.

[14] A.M. Baker, S.K. Babu, R. Mukundan, S.G. Advani, A.K. Prasad, D. Spernjak, R. L. Borup, Cerium ion mobility and diffusivity rates in perfluorosulfonic acid membranes measured via hydrogen pump operation, J. Electrochem. Soc. 164 (2017) F1272–F1278, https://doi.org/10.1149/2.1221712jes.

[15] K.H. Wong, E. Kjeang, In-Situ modeling of chemical membrane degradation and mitigation in ceria-supported fuel cells, J. Electrochem. Soc. 164 (2017) F1179–F1186, https://doi.org/10.1149/2.1201712jes.

[16] K. Shinozaki, In situ 2D-XAS imaging and modeling analysis of cerium migration in proton exchange membrane fuel cells in situ 2D-XAS imaging and modeling analysis of cerium migration in proton exchange membrane fuel cells, J. Electrochem. Soc. 172 (n.d.) 24505. https://doi.org/10.1149/1945-7111/adb2ea.

[17] M.A. Schilling, T. Lazaridis, V. Meier, M. Hanauer, In situ quantification of transition metal cation leaching from a Pt-Alloy cathode catalyst in a PEM fuel cell in situ quanti fi cation of transition metal cation leaching from a Pt-Alloy cathode catalyst in a PEM, Fuel Cell (2002), https://doi.org/10.1149/1945-7111/ada188.

[18] J.P. Braaten, X. Xu, Y. Cai, A. Kongkanand, S. Litster, Contaminant cation effect on oxygen transport through the ionomers of polymer electrolyte membrane fuel cells, J. Electrochem. Soc. 166 (2019) F1337–F1343, https://doi.org/10.1149/2.0671916jes.

[19] E. Colombo, A. Baricci, A. Bisello, L. Guetaz, A. Casalegno, PEMFC performance decay during real-world automotive operation: evincing degradation mechanisms and heterogeneity of ageing, J. Power Sources 553 (2023) 232246, https://doi.org/10.1016/j.jpowsour.2022.232246.

[20] L. Cheng, K. Khedekar, M. Rezaei Talarposhti, A. Perego, M. Metzger, S. Kuppan, S. Stewart, P. Atanassov, N. Tamura, N. Craig, I.V. Zenyuk, C.M. Johnston, Mapping of heterogeneous catalyst degradation in polymer electrolyte fuel cells, Adv. Energy Mater. 10 (2020) 1–7, https://doi.org/10.1002/aenm.202000623.

[21] Y.-H. Lai, K.M. Rahmoeller, J.H. Hurst, R.S. Kukreja, M. Atwan, A.J. Maslyn, C. S. Gittleman, Accelerated stress testing of fuel cell membranes subjected to combined mechanical/chemical stressors and cerium migration, J. Electrochem. Soc. 165 (2018) F3217–F3229, https://doi.org/10.1149/2.0241806jes.

[22] T. Agarwal, A.C. Sievert, S. Komini Babu, S. Adhikari, E.J. Park, A.K. Prasad, S. G. Advani, T.E. Hopkins, A.M. Park, Y.S. Kim, R.L. Borup, Enhancing durability of polymer electrolyte membrane using cation size selective agents, J. Power Sources 580 (2023) 233362, https://doi.org/10.1016/j.jpowsour.2023.233362.

[23] Y. Xing, L. Liu, Z. Fu, Y. Li, H. Li, High-performance and durable membrane electrode assemblies based on CeO2 and ePTFE double-reinforcement strategy for proton exchange membrane fuel cells operating at elevated temperatures, J. Power Sources 587 (2023) 233727, https://doi.org/10.1016/j.jpowsour.2023.233727.

[24] F. Verducci, A. Grimaldi, E. Colombo, A. Casalegno, A. Baricci, Dynamic modeling of polymer electrolyte membrane fuel cells under real-world automotive driving cycle with experimental validation on segmented single cell, Renew. Energy 234 (2024) 121194, https://doi.org/10.1016/j.renene.2024.121194.

[25] H. Matsui, S. Takao, K. Higashi, T. Kaneko, G. Samjeské, T. Uruga, M. Tada, Y. Iwasawa, Operando imaging of Ce radical scavengers in a practical polymer electrolyte fuel cell by 3D fluorescence CT-XAFS and depth-profiling Nano-XAFS-SEM/EDS techniques, ACS Appl. Mater. Interfaces 14 (2022) 6762–6776, https://doi.org/10.1021/acsami.1c22336.

[26] Z. Turtayeva, F. Xu, J. Dillet, K. Mozet, R. Peignier, A. Celzard, G. Maranzana, Manufacturing catalyst-coated membranes by ultrasonic spray deposition for PEMFC: identification of key parameters and their impact on PEMFC performance, Int. J. Hydrogen Energy 47 (2022) 16165–16178, https://doi.org/10.1016/j.ijhydene.2022.03.043.

[27] A.M. Baker, S. Komini Babu, K. Chintam, A. Kusoglu, R. Mukundan, R.L. Borup, Ce cation migration and diffusivity in perfluorosulfonic acid fuel cell membranes, ECS Meet. Abstr. MA2019-02 (2019), https://doi.org/10.1149/ma2019-02/34/1502, 1502–1502.

[28] E. Colombo, D. Casadei, A. Baricci, A. Casalegno, An open-source zero-gradient cell hardware to improve and accelerate durability testing of PEM fuel cells, HardwareX 16 (2023) e00495, https://doi.org/10.1016/j.ohx.2023.e00495.

[29] Link to manufacturer webpage. https://www.binder-world.com/int-en/products/incubators/cooling-incubators.

[30] V.A. Solé, E. Papillon, M. Cotte, P. Walter, J. Susini, A multiplatform code for the analysis of energy-dispersive X-ray fluorescence spectra, Spectrochim. Acta Part B At. Spectrosc. 62 (2007) 63–68, https://doi.org/10.1016/j.sab.2006.12.002.

[31] C.G. Ryan, E. Clayton, W.L. Griffin, S.H. Sie, D.R. Cousens, SNIP, a statistics-sensitive background treatment for the quantitative analysis of PIXE spectra in geoscience applications, Nucl. Instrum. Methods Phys. Res. B. 34 (1988) 396–402, https://doi.org/10.1016/0168-583X(88)90063-8.

[32] Link to manufacturer webpage. https://info.tescan.com/micro-ct.

[33] K. Morita, A. Takezawa, N. Kitano, A. Kuwaki, A. Kato, S. Yamaguchi, K. Shinozaki, Y. Orikasa, In-situ X-ray fluorescence analysis of In-plane cerium-ion distribution under humidity gradients in proton exchange membrane, ECS Meet. Abstr. MA2024-01 (2024), https://doi.org/10.1149/ma2024-01362104mtgabs, 2104–2104.

[34] G. Pourcelly, P. Sistat, A. Chapotot, C. Gavach, V. Nikonenko, Self diffusion and conductivity in NafionR membranes in contact with NaCl+CaCl2 solutions, J. Membr. Sci. 110 (1996) 69–78, https://doi.org/10.1016/0376-7388(95)00232-4.

[35] T. Okada, G. Xie, O. Gorseth, S. Kjelstrup, N. Nakamura, T. Arimura, Ion and water transport characteristics of nafion membranes as electrolytes, Electrochim. Acta 43 (1998) 3741–3747, https://doi.org/10.1016/S0013-4686(98)00132-7.

[36] A.Z. Weber, C. Delacourt, Mathematical modelling of cation contamination in a proton-exchange membrane, Fuel Cells 8 (2008) 459–465, https://doi.org/10.1002/fuce.200800044.

[37] T.T.H. Cheng, J.E. Soc, T.T.H. Cheng, S. Wessel, S. Knights, Interactive effects of membrane additives on PEMFC catalyst layer degradation interactive effects of membrane additives on PEMFC catalyst layer degradation. https://doi.org/10.1149/2.056301jes, 2013.

[38] D. Banham, S. Ye, T. Cheng, S. Knights, S.M. Stewart, Effect of CeOx crystallite size on the chemical stability of CeOx nanoparticles effect of CeOx crystallite size on the chemical stability of CeOx, (n.d.). https://doi.org/10.1149/2.0931410jes.

[39] S. Shi, A.Z. Weber, A. Kusoglu, Structure/Property relationship of nafion XL composite membranes, J. Membr. Sci. 516 (2016) 123–134, https://doi.org/10.1016/j.memsci.2016.06.004.

[40] L. Thilo, M. Thomas, S. Nina, G. Jonas, D2.4: Final Protocol Definition for Heavy-Duty Accelerated Stress Tests and Load Profile Tests, 2023, pp. 4–5.

[41] Y.-H. Lai, K.M. Rahmoeller, J.H. Hurst, R.S. Kukreja, M. Atwan, A.J. Maslyn, C. S. Gittleman, Accelerated stress testing of fuel cell membranes subjected to combined mechanical/chemical stressors and cerium migration, J. Electrochem. Soc. 165 (2018) F3217–F3229, https://doi.org/10.1149/2.0241806jes.

[42] V. Liso, S. Simon Araya, A.C. Olesen, M.P. Nielsen, S.K. Kær, Modeling and experimental validation of water mass balance in a PEM fuel cell stack, Int. J. Hydrogen Energy 41 (2016) 3079–3092, https://doi.org/10.1016/j.ijhydene.2015.10.095.

[43] T. Berning, A. Olesen, S. Kær, On the diffusion coefficient of water in polymer electrolyte membranes, ECS Meet. Abstr. MA2012-02 (2012), https://doi.org/10.1149/ma2012-02/13/1556, 1556–1556.

[44] A. Kusoglu, A.Z. Weber, Water transport and sorption in nafion membrane, ACS Symp. Ser. 1096 (2012) 175–199, https://doi.org/10.1021/bk-2012-1096.ch011.

[45] A. Grimaldi, A. Baricci, S. De Antonellis, C. Oldani, A. Casalegno, Experimental study and modeling of water transport through short-side-chain perfluorosulfonic acid membranes, J. Power Sources 558 (2023) 232556, https://doi.org/10.1016/j.jpowsour.2022.232556.

[46] A. Goshtasbi, B.L. Pence, J. Chen, M.A. DeBolt, C. Wang, J.R. Waldecker, S. Hirano, T. Ersal, A mathematical model toward real-time monitoring of automotive PEM fuel cells, J. Electrochem. Soc. 167 (2020) 24518, https://doi.org/10.1149/1945-7111/ab6dd1.

[47] PhD Thesis, Politecnico di Milano, A. Grimaldi, Modelling and experimental analysis of PEM fuel cells under dynamic real-world conditions focusing on the design of an air humidifier. https://www.politesi.polimi.it/handle/10589/206693, 2023.

[48] F. Wilhelm, E. Colombo, A. Bisello, A. Baricci, A. Casalegno, F. Micoud, S. Escribano, K. Talukdar, P. Gazdzicki, ID-FAST - Investigations on Degradation Mechanisms and Definition of Protocols for PEM Fuel Cells Accelerated Stress Testing, D4.3 – Analysis of Coupling Between Mechanisms and Definition of Combined Asts, 2021, p. 49. https://www.id-fast.eu/uploads/media/ID-FAST_D4-3_Analysis_of_coupling_between_mechanisms_and_definition_of_combined_ASTs_OK.pdf.

[49] C. Rabissi, P. Gazdzicki, L. Guétaz, S. Escribano, L. Grahl-Madsen, A. Baricci, A. Casalegno, A locally resolved investigation on direct methanol fuel cell uneven components fading: steady state and degradation local analysis, J. Power Sources 397 (2018) 361–373, https://doi.org/10.1016/j.jpowsour.2018.07.034.

[50] E. Colombo, A. Bisello, A. Casalegno, A. Baricci, Mitigating PEMFC degradation during start-up: locally resolved experimental analysis and transient physical modelling, J. Electrochem. Soc. 168 (2021) 54508, https://doi.org/10.1149/1945-7111/abf4eb.

[51] A.M. Baker, D. Torraco, E.J. Judge, D. Spernjak, R. Mukundan, R.L. Borup, S. G. Advani, A.K. Prasad, Cerium migration during PEM fuel cell assembly and operation, ECS meet. abstr. MA2015-02, 1495–1495, https://doi.org/10.1149/ma2015-02/37/1495, 2015.

[52] E. Colombo, A. Casalegno, L. Guetaz, A. Baricci, Revealing the critical role of low voltage excursions in enhancing PEM fuel cell catalyst degradation by automotive hydrogen/air potential cycling experiments, Int. J. Hydrogen Energy 65 (2024) 292–307, https://doi.org/10.1016/j.ijhydene.2024.03.373.

[53] L.R. Johnson, X. Wang, C. Quesada, X. Wang, R. Mukundan, R. Ahluwalia, Chemical stability of PFSA membranes in heavy-duty fuel cells: fluoride emission rate model, Electrochemistry 6 (2025) 25, https://doi.org/10.3390/electrochem6030025.

[54] J. Choi, T. Kwon, Recent advances in ceria-based free radical scavenging nanoparticles for durability enhancement of polymer electrolyte membrane fuel cells, CrystEngComm 27 (2025) 5222–5237, https://doi.org/10.1039/d5ce00400d.

[55] T. Agarwal, A.C. Sievert, S. Komini Babu, S. Adhikari, E.J. Park, A.K. Prasad, S. G. Advani, T.E. Hopkins, A.M. Park, Y.S. Kim, R.L. Borup, Enhancing durability of polymer electrolyte membrane using cation size selective agents, J. Power Sources 580 (2023) 233362, https://doi.org/10.1016/j.jpowsour.2023.233362.

[56] H. Oh, B. Son, S. Shanmugam, Cerium-based perovskite mixed metal oxide as the radical scavenger for PEM fuel cells operating under low humidity conditions, ACS Appl. Mater. Interfaces 15 (2023) 28093–28105, https://doi.org/10.1021/acsami.3c04216.